

## Manuscript Details

<b>Manuscript number</b>	ADWR_2018_119
<b>Title</b>	Numerical Investigation of Viscous Flow Instabilities in Multiphase Heterogeneous Porous Media
<b>Article type</b>	Research Paper

### Abstract

A critical aspect of multiphase flow in porous media is the displacement efficiency that measures the amount of fluid that can be pushed by another fluid driven by pressure gradient. Migration of contaminants and reservoir waterflooding are typical applications where understanding the dynamics of immiscible fluid displacement helps mitigating water resources contamination and improving hydrocarbons production, respectively. Due to large viscosity ratios, flow instabilities at fluids' interface may arise leading to the formation of fingers -- uneven front with elongation at the outside edge of fluids interface, with strong impact on the displacement efficiency. Initial studies of viscous instabilities in Hele-Shaw cells indicated that the development of fingers mostly depends on mobility ratio and capillary number, however heterogeneity of the porous domain may also affect the onset of instabilities. Therefore, the main aim of this work is to numerically investigate formation and growth of viscous fingers in heterogeneous porous media. The model used here is based on a novel control volume finite element method (CVFEM) formulation with a family of FE-pairs,  $\text{IPN}[n]\{m\}$  specially tailored for Darcian flows. Dynamic mesh adaptivity enables capturing fingers development whilst saving computational overheads. Numerical experiments were performed to investigate the impact of viscosity ratio and heterogeneity on Saffmann-Taylor instabilities. Numerical simulations demonstrated that the heterogeneity of the domain triggers the early-onset formation of fingers under prescribed viscosity ratio conditions. Also, effective numerical capture of growth (in particular, tip-splitting) and coalescence of dendritic finger branching induced by large viscosity ratio largely depends on mesh resolution at the fluids interface.

**Keywords** Multi-fluid flows; Porous media; Viscous Instabilities; Mobility Ratio.

**Corresponding Author** Konstantinos Christou

**Corresponding Author's Institution** University of Aberdeen

**Order of Authors** Konstantinos Christou, W.C. Radünz, B. Lashore, F.B.S. de Oliveira, Jefferson Gomes

**Suggested reviewers** Zhihua Xie, Francisco Marcondes, Kamy Sepehrnoori, Pablo Salinas, Shayan Tavassoli

## Submission Files Included in this PDF

### File Name [File Type]

Manuscript\_ViscousInstabilities\_KC.pdf [Manuscript File]

## Submission Files Not Included in this PDF

### File Name [File Type]

0 submission file.zip [LaTeX Source File]

To view all the submission files, including those not included in the PDF, click on the manuscript title on your EVISE Homepage, then click 'Download zip file'.

1  
2  
3  
4  
5  
6  
7  
8  
9 Numerical Investigation of Viscous Flow Instabilities in  
10 Multiphase Heterogeneous Porous Media

11  
12 K. Christou<sup>a</sup>, W.C. Radünz<sup>a,b</sup>, B. Lashore<sup>a</sup>, F.B.S. de Oliveira<sup>c</sup>, J.L.M.A.  
13 Gomes<sup>a,\*</sup>

14  
15 <sup>a</sup>*Mechanics of Fluids, Soils & Structures Group, School of Engineering, University of  
Aberdeen, UK*

16 <sup>b</sup>*Engineering School, Federal University of Rio Grande do Sul, Brazil*

17 <sup>c</sup>*Department of Exact and Technological Sciences, State University of Santa Cruz,  
Bahia, Brazil*

---

20  
21  
22 Abstract

23  
24 A critical aspect of multiphase flow in porous media is the displacement efficiency  
25 that measures the amount of fluid that can be pushed by another fluid driven by pressure gradient.  
26 Migration of contaminants and reservoir waterflooding are typical applications where understanding the dynamics of  
27 immiscible fluid displacement helps mitigating water resources contamination and improving hydrocarbons production, respectively.  
28 Due to large viscosity ratios, flow instabilities at fluids' interface may arise leading to the  
29 formation of fingers – uneven front with elongation at the outside edge of  
30 fluids interface, with strong impact on the displacement efficiency.  
31 Initial studies of viscous instabilities in Hele-Shaw cells indicated that the development of fingers mostly depends on mobility ratio and capillary number,  
32 however heterogeneity of the porous domain may also affect the onset of instabilities.  
33 Therefore, the main aim of this work is to numerically investigate formation and growth of viscous fingers in heterogeneous porous media.  
34 The model used here is based on a novel control volume finite element method  
35 (CVFEM) formulation with a family of FE-pairs,  $P_nDG-P_m$  specially tailored for Darcean flows.  
36 Dynamic mesh adaptivity enables capturing fingers development whilst saving computational overheads.  
37 Numerical experiments were performed to investigate the impact of viscosity ratio and heterogene-

---

38 \*Corresponding author.

39 Email address: jefferson.gomes@abdn.ac.uk (J.L.M.A. Gomes)

ity on Saffmann-Taylor instabilities. Numerical simulations demonstrated that the heterogeneity of the domain triggers the early-onset formation of fingers under prescribed viscosity ratio conditions. Also, effective numerical capture of growth (in particular, tip-splitting) and coalescence of dendritic finger branching induced by large viscosity ratio largely depends on mesh resolution at the fluids interface.

*Keywords:* Multi-fluid flows, Porous media, Viscous Instabilities, Mobility Ratio.

---

## 1. Introduction

Numerical investigation of multiphase flows in porous media have attracted the attention of the scientific community over the past 40 years. Characterisation of such fluid flows serves as the foundation of reservoir engineering and groundwater studies (White et al., 1981). Underground coal gasification is another important field of interest and, more recently, due to the role of green house gases (GHG) emissions in the global climate change, several research work have focused on CO<sub>2</sub> migration and trapping mechanisms in carbon capture utilisation and storage (CCUS) operations (Spycher et al., 2003; Self et al., 2012; Jiang, 2011).

Description of physics and mechanisms of multiphase porous media flows were reported by Wooding and Morel-Seytoux (1976) with focus on capillary pressure and flow regimes. A comprehensive review of force balances at the interface between immiscible fluids and resulting mechanisms for flow instabilities can be found in Homsy (1987). Flow instabilities can be classified as macroscopic and microscopic, the former is due to imposed boundary conditions, whereas the later is associated to local phenomena at the fluids interface (*e.g.*, Kelvin-Helmholtz and Saffman-Taylor instabilities, Saffman, 1959). This work focuses on flow instabilities in two-phase systems due to viscous and stress forces (often referred as viscous instabilities or viscous fingering, Section 3).

In oil and gas reservoir exploration, viscous and density instabilities are relatively common during water-injection processes. As water and oil interacts, the interface between these fluids moves creating an uneven or fingered flow profile (see Fig. 3). Viscous fingering results in inefficient flow sweeping which can bypass significant quantities of recoverable oil and may lead to

early breakthrough of water into neighbour production wells. Viscous instabilities are mainly controlled by the mobility ratio (MR) between displacing and displaced fluids. Other conditions that may also influence the severity of viscous fingering are: heterogeneity (*i.e.*, wide spatial porosity and/or permeability distribution), gravitational forces, anisotropic dispersion, non-monotonic viscosity profile etc (Budek et al., 2017; Nicolaides et al., 2015).

Multi-fluid flow dynamics in porous media are described by continuity and momentum (extended Darcy's law) conservative equations for each fluid (or phases) with coupling mass terms (*i.e.*, density and saturation) appearing in both sets of equations. Advanced numerical methods are in continuous development to accurately represent force balances in Darcian flows. Finite difference methods (FDM) have been extensively used in most industry-standard reservoir simulators (Aziz and Settari, 1986; Chen et al., 2005; Chang et al., 1990) with relative success. However, they are often limited to relatively simple geometries representing idealised geological formations through structured quadrilateral (2-D) and hexahedral (3-D) grid cells (Mlacnik et al., 2004; King and Mansfield, 1999). Additionally, FDM schemes often result in excessive numerical dispersion when strong heterogeneity (represented by permeability and porosity fields) is present (Chavent and Jaffré, 1986).

The geometrical flexibility associated with high-order numerical accuracy of finite element methods (FEM) has proven to be more efficient than FDM to solve fluid flow dynamics in complex geometries. Among FEM-based formulations for porous media, the control volume finite element methods (CVFEM, Fung et al., 1992) has been widely used as it can guarantee local mass conservation and high-order numerical accuracy as well as being able to use tetrahedral geometry-conforming elements. In traditional CVFEM formulations, pressure and velocity are interpolated using piecewise linear FE basis functions, while material properties and flow conditions (*e.g.*, phase saturation, density, temperature, species concentration etc) are represented with CV basis functions (Voller, 2009). Saturation equations are solved explicitly after solving for the dual pressure-velocity at each non-linear iteration (a detailed description of the implicit pressure explicit saturation, IMPES, formulation can be found in Chen et al., 2006; Lux and Anguy, 2012).

Since geometries are captured by finite elements, constructed control volumes typically extend on each side of the interface which may have different properties. Therefore, some average values of the coupled velocity-pressure

fields (defined in the FE space but projected onto the CV space) are applied across the CVs at these interfaces. These often lead to excessive numerical dispersion especially in highly heterogeneous media (represented by spatial-dependent permeability and porosity fields). In order to overcome such artificial numerical dispersion, a discontinuous hybrid finite element finite volume method (DFEFVM) formulation was introduced by [Nick and Matthai \(2011a,b\)](#). This novel discretisation scheme was designed to simulate flows through discrete fractured rocks in which CVs are divided along the interfaces of different materials. [Cumming et al. \(2011\)](#) demonstrated that CVFEM discretisation could also be used to solve Richards' equations (coupled mass conservation and Darcy equation) in heterogeneous media with relatively small computational overhead (compared with traditional coupled velocity-pressure based formulations, see also [Cumming, 2012](#)). Fluxes over CVs were calculated based upon material properties, whereas the saturation field was volume-averaged at the interface of the materials, enforcing mass balance as described by [Kirkland et al. \(1992\)](#).

In this work, a novel CVFEM formulation, previously introduced by [Gomes et al. \(2017\)](#) (see also [Jackson et al., 2014; Salinas et al., 2015](#)), is used to numerically investigate formation and growth of viscous fingers in heterogeneous porous media. The continuity equation is embedded into the pressure equation to enforce mass conservation whilst ensuring that the force balance is preserved. A hybrid family of  $P_n$ DG- $P_m$  triangular and tetrahedral FE pairs is used to discretise velocity and pressure. A sketch of the  $P_1$ DG- $P_2$  FE-pair is shown in Fig. 1, in which velocity is represented by discontinuous and piecewise linear basis functions whereas pressure is interpolated through continuous and piecewise quadratic basis functions. Scalar fields are stored in CV space (Fig. 2). The dual pressure and velocity fields are represented simultaneously (through non-linear projections) in FE and CV spaces.

A brief description of the numerical formulation and viscous fluid instabilities are introduced in Sections 2 and 3, respectively. Model set up and results including initial model-benchmark are presented in Section 4. Impact of mobility ratio on the fingers formation is also included in this section. Finally, concluding remarks are presented in Section 5.

## 2. Model Formulation

The two-phase immiscible and incompressible fluid flow through a porous media domain  $\Omega$ , may be described by the coupled extended Darcy and

225  
226  
227  
228  
229  
230  
231  
232 saturation equations,

233  
234  
235 
$$\left( \frac{\mu_\alpha S_\alpha}{\mathbf{K} \mathcal{K}_{r\alpha}} \right) \mathbf{u}_\alpha = \underline{\sigma}_\alpha \mathbf{u}_\alpha = -\nabla p + \mathcal{S}_{u,\alpha} \quad \text{with } x_i \in \Omega, t > 0, \quad (1)$$

236  
237 
$$\phi \frac{\partial S_\alpha}{\partial t} + \nabla \cdot (\mathbf{u}_\alpha S_\alpha) = \mathcal{S}_{cty,\alpha} \quad \text{with } x_i \in \Omega, t > 0, \quad (2)$$

239 respectively, where  $\mu$ ,  $\mathbf{K}$ ,  $p$  and  $\phi$  are viscosity, absolute permeability, pressure and porosity, respectively.  $\mathbf{u}_\alpha$  is the saturation-weighted Darcy velocity of the  $\alpha$ -phase and  $\mathcal{K}_{r,\alpha}$  is the relative permeability.  $\mathcal{S}$  is the source term associated with the Darcy and continuity equations.  $S_\alpha$  represents the saturation of the  $\alpha$ -phase with mass conservation constraints of  $\sum_{\alpha=1}^{\mathcal{N}_p} S_\alpha = 1$ , where  $\mathcal{N}_p$  denotes the number of phases.  $\underline{\sigma}_\alpha$  is an absorption-like term that represents the implicit linearisation of the viscous frictional forces.

240 The formulation introduced here is applicable to  $\mathcal{N}_p$  fluid phases and  
241 is based on two families of FE-pairs:  $P_n$ DG- $P_m$ DG and  $P_n$ DG- $P_m$  (Cotter  
242 et al., 2009), consistent with the dual pressure-velocity representation in CV  
243 space. In these families of FE-pairs, velocity is represented by  $n^{\text{th}}$ -order  
244 polynomials that are discontinuous across elements, whereas pressure is rep-  
245 presented by  $m^{\text{th}}$ -order polynomials that may be either continuous or discon-  
246 tinuous (thus the notation  $P_n$ DG- $P_m$  and  $P_n$ DG- $P_m$ DG, respectively) across  
247 elements. Mass balance (continuity) equations are solved in CV space and a  
248 Petrov-Galerkin FEM is used to obtain high-order fluxes on CV boundaries,  
249 which are limited to yield bounded fields (*e.g.*, positive densities, saturations  
250 bounded between 0 and 1, etc). Simulations performed for this work were  
251 conducted using two types of elements:  $P_1$ DG- $P_1$  and  $P_1$ DG- $P_2$ .

252 Finite element basis functions for velocity and pressure fields are intro-  
253 duced in the discretisation of force-balance equations. Hybrid basis functions  
254 are also used to allow CV-based velocity to be extrapolated across the entire  
255 element. The extended Darcy equation (Eqn. 1) is discretised using a FE  
256 representation of  $\mathbf{v}_\alpha = \underline{\sigma}_\alpha \mathbf{u}_\alpha$  and  $p$  with FE basis functions  $Q_j$  and  $P_j$ , re-  
257 spectively – note that  $\underline{\sigma}_\alpha$  lies in both CV and FEM spaces. Each component  
258 of the weak form of the extended Darcy equation is tested with the  $\mathbf{v}_\alpha$  basis

function,  $Q_j$ , to obtain:

$$\sum_E \int_{\Omega_E} Q_i (\mathbf{v}_\alpha + \nabla p - \mathbf{s}_{u_\alpha}) dV + \oint_{\Gamma_E} Q_i \mathbf{n} (p - \tilde{p}) d\Gamma + \oint_{\Gamma_\Omega} Q_i \mathbf{n} (p - p_{bc}) d\Gamma = \mathbf{0}, \quad (3)$$

where  $\Omega_E$  and  $\Gamma_E$  are the volume and boundary of element  $E$ , respectively, and  $\Gamma_\Omega$  is the boundary of the computational domain. The numerical pressure  $\tilde{p}$  appearing in the jump condition (second term in Eqn. 3) is the arithmetic mean of the potentially discontinuous pressure across the element  $E$  (consistent with the  $P_n$ DG- $P_m$ DG element-pairs). This term vanishes when a continuous formulation is used to discretise the pressure field (with  $P_n$ DG- $P_m$  element-pairs). The last term in Eqn. 3 is used to weakly enforce the pressure level to  $p_{bc}$  on a computational domain boundary.

Whilst saturation (and all saturation-dependent material properties such as relative permeability and capillary pressure) is calculated in CV space, absolute permeability is assumed piecewise constant in FE space. Saturation equations (Eqn. 2) are discretised in space with CV basis function,  $M_i$ , and with the  $\theta$ -method in time (Gomes et al., 2012). Velocities across CV interfaces (within and between elements) are calculated through a directional-weighted flux-limited scheme based on upwind value of  $\sigma$  at individual CV as described by Jackson et al. (2013). Summing the discretised Eqn. 2 over all phases yields the global mass balance equation,

$$\sum_{\alpha=1}^{N_p} \left\{ \int_{\Omega_{CVi}} M_i \frac{\phi (S_{\alpha i}^{n+1} - S_{\alpha i}^n)}{\Delta t} dV + \oint_{\Gamma_{CVi}} [\theta^{n+1/2} \mathbf{n} \cdot \mathbf{u}_\alpha^{n+1} S_\alpha^{n+1} + (1 - \theta^{n+1/2}) \mathbf{u}_\alpha^n S_\alpha^n] d\Gamma - \int_{\Omega_{CVi}} M_i \mathcal{S}_{cty,\alpha}^{n+\theta} dV \right\} = 0, \quad (4)$$

where  $\Omega_{CVi}$  and  $\Gamma_{CVi}$  are the volume and boundary of CV  $i$  respectively,  $M_i$  are CV basis functions,  $\mathbf{n}$  is the outward pointing unit normal vector to the surface of  $CV_i$  and  $n$  is the current time level.  $\theta$  varies smoothly between 0.5 (corresponding to Crank-Nicolson method) and 1 (corresponding

337  
338  
339  
340  
341  
342  
343  
344  
345  
346  
347  
348  
349  
350  
351  
352  
353  
354  
355  
356  
357  
358  
359  
360  
361  
362  
363  
364  
365  
366  
367  
368  
369  
370  
371  
372  
373  
374  
375  
376  
377  
378  
379  
380  
381  
382  
383  
384  
385  
386  
387  
388  
389  
390  
391  
392

to backward-Euler scheme) to avoid the introduction of spurious oscillations for large grid Courant numbers.

The discretised global mass and force balance equations are solved using a multigrid-like approach as described by Pavlidis et al. (2016) (see also Salinas et al., 2016). The numerical formulation is fully described by Gomes et al. (2017) (see also Salinas et al., 2015; Adam et al., 2016).

### 3. Brief Summary of Viscous Instabilities

The study of viscous flow instabilities (*i.e.*, fingering) is particularly important in oil exploration due to heterogeneities (*i.e.*, natural fractures, permeability and/or porosity characteristics in different zones) of geological formations. A major problem associated with water-flooding processes is the early water-breakthrough caused by high-permeability layers and unfavorable mobility ratios. Water breakthrough and volumetric sweep efficiency (ratio of volumes between the recovered and the injected fluids) are the main determinants of the productive life of a reservoir (Riaz and Tchelepi, 2004; Tavassoli et al., 2015). During immiscible CO<sub>2</sub>-flooding (*i.e.*, in CO<sub>2</sub> enhanced oil recovery, CO<sub>2</sub>-EOR, processes), viscosity of supercritical CO<sub>2</sub> is lower than crude oil, thus viscous fingering and/or channelling may occur.

The efficiency of fluid displacement depends upon the ratio of viscous and capillary forces (or capillary number,  $N_c$ , Eqn. 5). When viscous force of the injected fluid overcomes the capillary force, hydrodynamic instabilities may occur, resulting in the collapse of the interface between fluids and fingers start to form.

Viscous flow instabilities can be found across several disciplines and scales, from chemical separation processes to geological reservoir fluids. Muskat (1934) investigated fluid flow in Hele-Shaw cells, *i.e.*, parallel flat plates separated by an infinitesimal gap, and the impact on the capillary number ( $N_c$ ),

$$N_c = \frac{\mu U}{\gamma}. \quad (5)$$

In Eqn. 5,  $\gamma$  is the surface tension and  $U$  is the characteristic velocity of the moving interface. This experimental apparatus enables instabilities to be qualitatively investigated by simplifying the flow in both porous and non-porous media into a 2D problem.

More recently, Howison (2000) and Praud and Swinney (2005) provided a comprehensive description of the mathematical formulation of immiscible two-phase flows in Hele-Shaw cells (also known as Saffman & Taylor problem). For a Hele-Shaw cell of a given size, flow development depends only on the capillary number. Thus if  $N_c$  is too high, Saffman (1959), Homsy (1987) and Tabeling et al. (1987) determined that the flow develops into a single steady-state finger which moves through the cell with constant velocity  $U$ .

Under the assumption that fluids remain immiscible along an interface, surface tension plays an important role in determining the shape and progress of the fingers (Howison, 2000). During the displacement of a fluid by a less viscous one, the expected uniform front (Buckley and Leverett, 1942; Sheldon and Cardwell, 1959) is perturbed leading to an uneven front with elongations at the outside edge of the fluid interface (Fig. 3), often referred as *fingers*. In homogeneous domains, fingers start to develop when the surface tension acting on the interface between the fluids exert an opposite force towards the change of shape of the interface. The interface becomes unstable and collapses, taking a curved shape (Homsy, 1987; Jackson et al., 2017).

In heterogeneous domains, such instability may be triggered by permeability differences across regions as demonstrated in Section 4.3. The higher the velocity of the low viscosity fluid, the less wide (tip-splitting behaviour) the finger is. Pressure differences acting on the interface produces a net pressure force,

$$\Delta P = -\gamma \nabla \cdot \hat{n}. \quad (6)$$

This expression is also known as the Young-Laplace equation, a relation describing the capillary pressure across the interface between two fluids, with  $\Delta P$  denoting the pressure difference and  $\hat{n}$  is the unit normal vector out of the surface.

As demonstrated by Habermann (1960) (see also Budek et al., 2017), mobility ratio (MR) is a key-parameter to assess fluid displacement and is defined as the ratio of mobility of the displacing (fluid  $i$ ) to that of the displaced fluid ( $j$ ),

$$MR = \frac{\mathcal{K}_{ri}\mu_j}{\mathcal{K}_{rj}\mu_i}. \quad (7)$$

MR is a function not only of fluids' viscosity and saturation, but also of the parameterised relative permeability,  $\mathcal{K}_{r\alpha}$ , which is often expressed as a function of local, residual and maximum phase saturations prescribed in the

pore rock matrix. In the simulations conducted for this work, the modified Brooks and Corey (1964) model was used (Alpak et al., 1999),

$$\mathcal{K}_{rw}(S_w) = \mathcal{K}_{rw}^o \left[ \frac{S_w - S_{w,irr}}{1 - S_{w,irr} - S_{nw,r}} \right]^{n_w}, \quad (8)$$

$$\mathcal{K}_{rnw}(S_{nw}) = \mathcal{K}_{rnw}^o \left[ \frac{S_{nw} - S_{nw,r}}{1 - S_{w,irr} - S_{nw,r}} \right]^{n_{nw}}, \quad (9)$$

where subscripts  $w$  and  $nw$  stand for wetting and non-wetting phases, respectively.  $\mathcal{K}_{rw}^o$  and  $\mathcal{K}_{rnw}^o$  are end-point relative permeability to wetting and non-wetting phases,  $S_{w,irr}$  and  $S_{nw,r}$  are irreducible wetting and residual non-wetting phase saturations, respectively. Exponents  $n_w$  and  $n_{nw}$  are both set to 2.

From Eqns. 7-9, it is clear that during fluid displacement, the mobility ratio changes as phase saturation,  $S_w(x_i, t)$  and  $S_{nw}(x_i, t)$ , varies in time and space (Eqn. 2). Therefore, with no lack of generality, the MR can be reduced to the viscosity ratio (VR),

$$VR = \frac{\mu_i}{\mu_j},$$

that will be used in the parametrisation of the numerical simulations conducted in Section 4. Analysis performed in the following sections will make use of this simplified definition as phase saturation ( $S_\alpha$ ) is a time- and spatial-dependent prognostic field which is calculated along with pressure ( $p$ ) and velocity ( $\mathbf{u}_\alpha$ ) fields.

In immiscible displacements, viscous fingering occurs when the viscosity ratio is greater than unity. As surface tension becomes weak, the interface is stressed and becomes unstable leading to the formation of fingers. At this point it should be mentioned that there are two parameters – Peclet number (Pe) and mobility ratio (MR), that determine the flow stability characteristics. There are always a few dominant fingers that spread and shield the growth of other fingers. The interface of the main finger collapses and starts splitting into new lobes of fingers. One of these new fingers may eventually outgrow the others and then spreads to occupy an increasingly larger width. In the process, the finger reaches a critical width while the saturation of its front becomes steep as a result of stretching caused by the cross-flow, causing the tip of the finger to become unstable and splits again, and the

505  
506  
507  
508  
509  
510  
511  
512 pattern repeats itself. Therefore, surface tension plays an essential dual role,  
513 it must be weak enough for the tip front to be unstable, but it is also the  
514 physical force causing the spreading and ensuing repeated branching (Tan  
515 and Homsy, 1988; Carvalho et al., 2013).

516 In the next section, the numerical formulation used to simulate multi-  
517 fluid flow in porous media is briefly validated (Section 4.2) against labora-  
518 tory experiments (qualitative validation). The impact of VR (quantitative  
519 validation) and heterogeneity on the onset instability and growth of fingers  
520 are numerically investigated in Section 4.3. Section 4.4 demonstrates the im-  
521 portance of an appropriate mesh resolution to adequately capture the initial  
522 stages of viscous fingers formation and development. Finally, flow pathway  
523 (channelling) is the focus of Section 4.5.

## 524 4. Results

### 525 4.1. Model Set-up

526 Numerical simulations were conducted with the model summarised in  
527 Section 2 and embedded in the next-generation flow simulator Fluidity/IC-  
528 FERST model software<sup>1</sup> (a full description of the model can be found in  
529 Jackson et al., 2013; Gomes et al., 2017). This multi-physics model has been  
530 validated against traditional multi-fluids test-cases (*e.g.*, advection-diffusion,  
531 Buckley-Leverett problem, channel model, immiscible displacement, gravity-  
532 driven displacement etc) in Radünz et al. (2014), Jackson et al. (2014), Salin-  
533 as et al. (2015) and Pavlidis et al. (2016).

534 In this work, all test-cases were performed in idealised geometries dis-  
535 cretised with unstructured triangular and tetrahedral mesh using the P<sub>1</sub>DG-P<sub>2</sub>  
536 and P<sub>1</sub>DG-P<sub>1</sub> FE-pairs (Fig. 2). An implicit Crank-Nicolson time-stepping  
537 scheme was used with *a posteriori* adaptive time-step size targeting a maxi-  
538 mum Courant-Friedrichs-Lowy condition (CFL, Courant et al., 1941) of 2. In  
539 most simulations, the domain was initially fully saturated with non-wetting  
540 fluid which was displaced by a pure (wetting) fluid at a prescribed initial  
541 velocity ( $u^0$ ). For simplicity, the porosity ( $\phi$ ) of the domain was kept con-  
542 stant at 0.2 in all simulations, whereas the absolute permeability ( $\mathbf{K}$ ) varied  
543 in space, *i.e.*,  $\mathbf{K} = \mathbf{K}(x_i)$ . Fluids are assumed incompressible and gravity

---

551  
552 <sup>1</sup><http://multifluids.github.io>

561  
562  
563  
564  
565  
566  
567  
568 was neglected. Initial set-up for the numerical simulations is summarised in  
569 Table 1.  
570

#### 571 4.2. Initial Model Validation

572 Numerical simulations (based on lab experiments due to [Evans and Dawe, 1994](#);  
573 [Dawe and Grattoni, 2008](#)) were conducted to demonstrate the model  
574 capability to capture viscous crossflow during immiscible displacement in  
575 heterogeneous porous media. The 2D domain, shown in Fig. 4, is  $4 \times 2$   
576 unit-length and fully saturated with fluid 2 ( $VR=1$ ). Fluid 1 is injected from  
577 the left-hand side of the domain with constant velocity of  $u = 1$ . Boundary  
578 conditions also include no-flux across upper and lower borders. The domain  
579 consists of four regions in which each quarter is represented by a permeability  
580 value, Fig. 4(a). The spatial permeability distribution creates a rough pres-  
581 sure field, *i.e.*, pressure gradient is discontinuous across the interface between  
582 different permeability zones, thus the fluid flows to the larger permeability  
583 region.  
584

585 A two-phase immiscible flow along homogeneous and parallel layers of  
586 contrasting petrophysical properties (*i.e.*, permeability) is initially simulated.  
587 During the fluid displacement, crossflow between adjacent layers often occur  
588 due to viscous, capillary and/or gravitational forces that drive the flow. In  
589 this numerical simulation, crossflow is caused by viscous forces, which is com-  
590 monly named viscous crossflow. Figures 4(b) and (c) show the continuous  
591 displacement of fluid 2 due to the injection of fluid 1. They also demonstrate  
592 the preferential flow path through high-permeability regions. Such flow be-  
593 haviour, represented by the crossflow through the four regions, is in good  
594 qualitative agreement with experiments conducted by [Dawe and Grattoni](#)  
595 ([2008](#)).  
596

#### 597 4.3. Flow Simulations in Hele-Shaw Cells at Different Viscosity Ratio Con- 598 ditions

599 In order to investigate the impact of viscosity ratio on the flow dynamics,  
600 numerical simulations of fluid displacement were conducted in Hele-shaw cells  
601 following the work of [Saffman \(1986\)](#). In this manuscript, the onset of viscous  
602 flow instabilities (following his seminal work in [Saffman and Taylor, 1958](#)) is  
603 investigated along with the impact of boundary conditions in the problem's  
604 mathematical formulation and solutions.  
605  
606

617  
 618  
 619  
 620  
 621  
 622  
 623  
 624 Here, 2D simulations were conducted in a  $5 \times 5$  cm domain (Fig. 5a) fully  
 625 saturated with a fluid. Wetting phase fluid is driven from the bottom left-  
 626 hand corner of the domain with velocity of  $1 \text{ cm.s}^{-1}$  (magnitude). No-flux  
 627 boundary conditions were imposed to all borders of the domain except at the  
 628 top right-hand side corner (named as sink), and a pressure gradient between  
 629 source and sink regions was initially imposed to the system.  
 630

631 Figures 5-7 show fluid displacement in simulations conducted with  $VR =$   
 632  $\{3, 10, 150\}$ , respectively. At relatively low viscosity ratio conditions (*i.e.*,  
 633  $VR=3$ ), saturation evolves in time with a smooth front throughout most of  
 634 the domain, and no finger could be observed. Elongated saturation profile  
 635 at later stages of the simulation is due to pressure gradient near the sink  
 636 region. However, formation of fingers can be readily noticed at early stages  
 637 of simulations conducted with viscosity ratios of 10 and 150.  
 638

639 Viscous finger morphologies were investigated by [Guan and Pitchumani \(2003\)](#)  
 640 based on mathematical formulation and semi-analytic solutions of the  
 641 coupled Darcy and continuity equations developed by [McLean and Saffman \(1981\)](#).  
 642 They conducted a sensitivity analysis to investigate fingers' formation,  
 643 dimensions and branchiness for a range of viscosity ratios ( $10^2 \leq VR \leq 10^4$ )  
 644 and modified capillary numbers ( $632 \leq N'_C \leq 6.32 \times 10^7$ , with  
 645  $N'_C = U_f \mu \gamma^{-1} (W/b)^2$ , where  $U_f$  is the velocity of the finger,  $W$  is half Hele-  
 646 Shaw cell width and  $b$  is the cell thickness). Finger width ( $\lambda_f$ ) and volumetric  
 647 flow rate ( $Q$ ) at the outflow region are correlated through,  
 648

$$649 \quad Q = U_f b \lambda_f. \quad (10) \\ 650$$

651 Here, numerical simulations performed with viscosity ratio of 10 and 150  
 652 indicated maximum fingers width of approximately 0.45-0.70 and 0.50-0.90  
 653 cm (Fig. 8 a and b), respectively. This is in close agreement with expected  
 654 values obtained from Eqn. 10 which indicates maximum finger width ranging  
 655 from 0.13 to 0.75 (for  $VR=10$ ) and from 0.30 to 0.75 ( $VR=150$ , Table 2).  
 656

657 Fluid flow dynamics through heterogeneous porous media are sensibly  
 658 more complex than in homogeneous media and strongly depend on problem  
 659 properties. Studies by [Langtangen et al. \(1992\)](#) on fluid flow dynamics  
 660 in heterogeneous porous media (analytical and numerical solutions) demon-  
 661 strated that hyperbolic Buckley-Leverett model is inherently unstable, *i.e.*,  
 662 the expected uniform interface front collapses as any perturbation in phys-  
 663 ical parameters are imposed to the problem. Spatial variation in geological  
 664

formations occurs in all length-scales, where heterogeneity characteristics in small length-scales (*i.e.*, pore) are statistically embedded into permeability (absolute and relative) and porosity parameters. Such multi-scale heterogeneity induces preferential flow pathways and plays a significant role in the onset of fluid instabilities as it triggers fingers formation and their accelerated growth (see Wing et al., 1989; Tchelepi and Jr, 1994).

In order to qualitatively investigate the impact of heterogeneity (here represented by changing in the permeability field), numerical simulations were conducted using a prescribed permeability distribution and viscosity ratios of 10 and 150. Absolute permeability ranging from  $1.0 \times 10^{-12}$  to  $5.0 \times 10^{-10}$  cm<sup>2</sup> (*i.e.*,  $0.1 \leq K \leq 50$  millidarcy) was used in the simulations, which were performed with the same geometry, mesh resolution, boundary and initial conditions as in previous homogeneous cases(Figs. 5-8b).

Figures 9 and 10 show formation of multi-scale elongations with continuous growth and coalescence of dendritic finger branching in simulations performed with viscosity ratio of 10 and 150, respectively. In both simulations, maximum fingers width of approximately 0.44-0.56 ( $VR=10$ ) and 0.24-0.44 cm were found, whereas estimated values (based on Eqn. 10) were 0.25-4.50 ( $VR=10$ ) and 0.88-3.00 cm ( $VR=150$ ) – Fig. 8 c-d, Table 2. Such calculated ranges (*i.e.*, theoretical values based on analytic solutions due to McLean and Saffman, 1981) clearly overestimate fingers dimensions as the mathematical formulation (and therefore Eqn. 10) assumes incompressible flows in homogeneous porous medium, *i.e.*, it does not take into account any spatial variability of heterogeneity.

#### 4.4. Capturing Flow Dynamics and Fingering Growth: Impact of Mesh Resolution

In most numerical simulations involving geo-fluid dynamics, local geometric constraints (*e.g.*, faults, fractures etc) and spatial multi-scale variability of flow properties are often ignored as the underlying computational mesh grid is too coarse to reliably represent any of these features. Whilst structured grids often struggle to conform to complex domain boundaries with consistent mesh connectivity, unstructured mesh techniques often relax cells' neighbourhood relationship constraints by dividing the domain into polytopes in which elements share adjacent faces. This leads to mesh grids that conform to the domain topography and can make the best use of state-of-the-art self-adaptive computational methods.

In Section 4.3, the impact of viscosity ratio on the growth of fingers and the triggering effect of heterogeneity on instability's nucleation were demonstrated in modified simulated Hele-Shaw cells. In order to capture the continuous development of viscous instabilities, mesh grids with sufficient resolution need to be applied over the interface between fluids. Figure 11 shows a numerical simulation performed with the same geometry, boundary and initial conditions as the one shown in Fig. 10, but with noticeable lower resolution (3734 instead of 26313 elements). As it can be seen, the lower the resolution the more difficult is to capture the fingers formations, growth and branching.

Traditional computational geo-fluid dynamics (CGFD) models often rely on fixed mesh with sufficient resolution throughout the domain to capture specific flow dynamics (*e.g.*, fluid instabilities, flow re-circulation, heat and mass transfers etc), however computational overhead may be prohibitive for simulations involving complex geometries and heterogeneous properties. Mesh adaptivity methods have been extensively used by the CGFD community to help capturing detailed flow dynamics, compositional non-equilibrium fluid displacement and solid-fluid interactions (Paluszny et al., 2007; Pietro et al., 2014; Su et al., 2016; Melnikova et al., 2016). In these methods, the mesh grid is continuously modified (*i.e.*, adjustments of the number and distribution of the degrees of freedom to reduce solution error) to focus resolution where is necessary as the simulation evolves in time and space. There are four main families of mesh adaptivity methods: adaptive mesh refinement (AMR), edge and face element manipulations whereas keeping the order of the element basis function fixed (h-adaptivity), mesh deformation (r-adaptivity) and changes of element basis function order (p-adaptivity). Detailed description and analysis of mesh adaptivity methods are beyond the scope of this manuscript but can be readily found in Lo (2015) (see also Plewa et al., 2004; Frey and George, 2008).

The dynamic mesh adaptive algorithm embedded in the Fluidity/IC-FERST model utilises a metric tensor field dependent on solution interpolation error-estimates which locally control the topology of elements in the metric (Pain et al., 2001; Power et al., 2006). Mesh optimisation generates unstructured finer mesh in regions where flow properties change faster, and coarser mesh in regions where properties change more slowly (Piggott et al., 2006). The mesh adapts in three stages: metric formation, mesh optimisation and fields' interpolation from the pre- to post-adapted mesh (see Hiester

et al., 2014). In the simulations shown in this work, mesh will adapt as a response to oscillations in the phase saturation field with prescribed interpolation error estimate (Mostaghimi et al., 2016).

Here, two numerical simulations were conducted with fixed and adaptive mesh resolutions to qualitatively assess model capability to capture fingers dynamics. In order to trigger the formation of fingers, regions with sharp permeability gradient were introduced. The computational domain, Fig. 12a, consists of a rectangular geometry fully saturated with a fluid (except by a squared region containing 50% of a second fluid – wetting fluid phase, Fig. 12b) and divided into 5 regions with prescribed permeability distribution. A no-flux boundary condition was imposed across upper and lower borders, whilst pure wetting fluid phase (*i.e.*,  $S_1 = 1$ ) is driven into the domain from the left-hand side face at velocity  $u_1 = 1$ . Viscosity ratio was set to 10.

Figures 13 and 14 show fluid displacement in simulations performed with fixed and adaptive meshes. Both simulations started with a mesh of 13068 triangular ( $P_1$ DG- $P_2$ ) elements, however as flow dynamics evolve the number of elements of the simulation conducted with adaptive mesh oscillates from a minimum of 4400 to a maximum of 16430 (Fig. 15). In both cases, fingers' development (formation, growth and coalescence) and fluid cross flows (through regions of distinct permeabilities at the top of the domain,  $\mathbf{K} = \{2, 3\}$ ) can be readily noticed. The simulation performed with a fixed and relatively fine mesh was able to capture the progressive development of fingers (as shown in Fig. 16b) prompted by sharp permeability gradient at the interface of regions with  $\mathbf{K} = \{1, 5\}$ . In regions with no permeability gradient, formation and development of fingers (Fig. 16c) were not captured by the simulation conducted with fixed mesh. In both cases, dynamic adaptive mesh based on perturbation of phase saturations with imposed interpolation error estimate proved to be able to capture the onset of instabilities and fingers' development with relatively little computational overhead, as indicated in Fig. 15.

#### 4.5. 3-D channel flows

In geological formations, preferential pathways flows may result in fast pollutant transport (advection-diffusion-dispersion) after industrial spillage (therefore leading to contamination of groundwater) or low hydrocarbon recovery rates (in water-,  $CO_2$ - and/or polymer-flooding operations in oil/gas

field exploration). In this Section, 3D simulations are conducted to investigate preferential flow pathways through semi-pervious and impervious geological layers.

The computational domain with permeability distribution of  $10^{-4} \leq K \leq 10^5$  milidarcy (Fig. 17) was designed to naturally capture preferential flow pathways through channels of large absolute permeability. Pure (wetting) fluid is added into the domain with uniform velocity of  $2.5 \text{ cm.s}^{-1}$  from the left-hand side face. No-flux boundary conditions are applied to all borders, except at the inlet (left-hand side) and outflow (right-hand side) faces. Initially, the domain was partially saturated with non-wetting fluid, *i.e.*,  $S_{nw}(t = 0) = 0.80$ , which was continuously displaced by the wetting fluid as the simulation progress. The domain was discretised with 235k tetrahedral P<sub>1</sub>DG-P<sub>1</sub>DG element-pairs.

As demonstrated in the preliminary model validation (Section 4.2), cross-flow towards the upper region of the initial part of the domain is due to boundary pressures and diffusivities (both at different vertical layers), *i.e.*, caused by large permeability gradients (Fig. 19). As the simulation progresses, non-wetting fluid is driven from regions with lower fluid resistance (central channel), although adjacent region (with low permeability) remains stagnant.

Such preferential flow pathways are clearly indicated in Fig. 18, where Darcy velocity vectors overlapped with wetting phase fluid saturation are shown. Fluid displacement occurs mainly in regions of relatively larger permeability, leaving other parts of the domain (*i.e.*, regions with low permeability distribution) with little or no momentum, indicating that at these regions the non-wetting fluid (*i.e.*, fluid 2) is not effectively displaced.

In Sections 4.3-4.4, finger's formation, growth and branching were triggered by domain heterogeneity represented by permeability differences. The progress of the saturation front and formation and growth of fingers in time and space can be seen in more details in isosurfaces (Fig. 20).

A similar numerical simulation (*i.e.*, same geometry, initial mesh resolution, initial and boundary conditions) was also performed using dynamically adaptive mesh. During the simulation, mesh resolution ranged from 235k to 643k P<sub>1</sub>DG-P<sub>1</sub>DG element-pairs (Fig. ??a). Distinct preferable flow pathways and fingers are shown in Fig. ??b-c and 23. Saturation of the wetting fluid during the course of the simulation is shown in Fig. 21. As expected,

both simulations (fixed and adaptive mesh, Figs. 19 and 21, respectively) led to similar results, *i.e.*, similar flow pathways and fingers development.

However, due to low-order accuracy of element-pairs –  $P_1DG-P_1DG$  instead of  $P_1DG-P_2$  of previous sections (for full investigation on numerical accuracy associated with these element-pairs, see Salinas et al., 2015, 2016, 2018; Adam et al., 2016; Gomes et al., 2017), and coarser mesh throughout the computational domain, simulation performed with fixed mesh showed larger smeared fluid saturation.

## 5. Conclusions

During immiscible multi-fluid flow displacements, the expected uniform front becomes unstable due to: (a) density ratio; (b) viscosity ratio, and; (c) heterogeneity. If viscosity ratio is relatively large ( $VR \geq 3$ ), surface tension becomes weak and the interface between two fluids is unstable in the presence of tangential velocity discontinuities, leading to the formation of fingers (Saffman, 1986). Heterogeneity in the porous media domain also leads to solution instabilities in the hyperbolic Buckley-Leverett problem (Langtangen et al., 1992). This paper aims to numerically investigate the dynamics of viscous flow instabilities in porous media triggered by permeability heterogeneity.

Simulations involving formation and growth of viscous fingers were conducted with the CVFEM-based multi-fluid flow simulator Fluidity/IC-FERST model. The model is based upon a dual consistent pressure-velocity representation in CV and FEM spaces and a novel family of FE-pairs,  $P_nDG-P_m$  and  $P_nDG-P_mDG$ . Saturation and other scalar fields are discretised in CV space and may be fully discontinuous across finite element boundaries. In order to strongly enforce discretised Darcy equations at the boundaries between elements and control volumes, a directional-weighted flux-limited was introduced to take into account discontinuities risen from both, numerical formulation (based on discontinuous-Galerkin finite element method, DGFEM) and control volumes within finite elements.

The numerical formulation was initially validated against laboratory experiments (Dawe and Grattoni, 2008) to qualitatively assess model functionality to simulate crossflow (*i.e.*, preferential flow pathways) in a chequerboard permeability domain. Formation and development of viscous fingers in Hele-Shaw cells (homogeneous domain) were investigated to demonstrate that the

onset of interface flow instability occur when  $VR \geq 3$ . Maximum dendritic finger widths obtained from numerical simulations performed with  $VR=10$  and  $VR=150$  largely agree with expected parametric analytic solutions ([McLean and Saffman, 1981](#); [Guan and Pitchumani, 2003](#)). However, when perturbations are imposed into the domain's geophysical properties, *i.e.*, spatial variability of absolute permeability, numerical solutions partially agree with analytic solutions (Table 2). This may be due to the domain homogeneity assumption in the analytic solution (Eqns. 10).

Determining the early-onset flow instability is critical to accurately simulate formation, growth and coalescence of fingers, and therefore to: (a) predict displacement (sweep) efficiency and (b) design strategies to either mitigate or avoid fingering and preferential flow pathways. Mesh resolution is thus crucial to investigate Saffmann-Taylor instabilities, and adaptive dynamic mesh technology has proved to be an efficient tool to capture initial interface perturbations. Numerical simulations were performed with  $VR=10$  using fixed and adaptive  $P_1DG-P_2$  element-pairs. Results (Figs. 15 and 16) demonstrated that by dynamically adapting the mesh to follow saturation gradients (*i.e.*, fluids interfaces), early-onset flow instability and further formation of long multi-fluid fingers, which have themselves split into sub-fingers, can be readily captured (see Figs. 13i and 14i). Overall computational cost of the simulation conducted with dynamically adapting the mesh were significantly smaller than the simulation conducted with fixed mesh as indicated by the number of elements/nodes (Figs. 15).

Investigation of preferential flow pathways was the focus of Section 4.5, where 3D numerical simulations of multi-fluid flow through semi-pervious / impervious channelised domain were performed. Numerical data indicated preferential flow through regions of larger permeability leaving adjacent region (with low permeability) with nearly stagnant fluids (Figs. 19- 18). Order of accuracy of the element-pair and mesh resolution play key-roles to capture directional flow pathways and fingers in 3D simulations.

This work focuses on complexity associated with flow channelling and instability dynamics in heterogeneous porous media. Methods used to simulate such flows are based in a novel high-order CVFEM formulation that accurately preserves sharp fluid saturation gradients associated with contrasting permeability distribution. Future work will include numerical investigation of (a) crossover from capillary fingering (at low fluid velocity) to viscous fingering for immiscible unstable flows, and (b) coupled viscous and density

1009  
1010  
1011  
1012  
1013  
1014  
1015  
1016 fingering in miscible fluid flows.  
1017  
1018

## 1019 6. Acknowledgements

1020 Mr William Radünz would like to acknowledge the support from the  
1021 Brazilian Research Council (CNPq) under the *Science without Borders schol-*  
1022 *arship programme*. Mr Konstantinos Christou would like to acknowledge the  
1023 support of the University of Aberdeen - College of Physical Science as well as  
1024 the Aberdeen Formation Evaluation Society (*AFES* is an SPWLA chapter).  
1025

1065  
1066  
1067  
1068  
1069  
1070  
1071  
1072

## References

- 1073 Adam, A., Pavlidis, D., Percival, J., Salinas, P., Xie, Z., Fang, F., Mug-  
1074 geridge, A., Jackson, M., 2016. Higher-order conservative interpolation  
1075 between control-volume meshes: Application to advection and multiphase  
1076 flow problems with dynamic mesh adaptivity. *Journal of Computational  
1077 Physics* 321, 512–531.
- 1078  
1079 Alpak, F., Lake, L., Embid, S., 1999. Validation of a modified carman-kozeny  
1080 equation to model two-phase relative permeabilities. In: SPE Annual Tech-  
1081 nical Conference and Exhibition. SPE, Texas, SPE56479.
- 1082  
1083 Aziz, K., Settari, A., 1986. Fundamentals of reservoir simulation. Elsevier  
1084 Applied Science Publishers, New York.
- 1085  
1086 Brooks, R., Corey, A., 1964. Hydrology Papers. Vol. 3. Colorado State Uni-  
1087 versity Press, Ch. Hydraulic properties of porous media.
- 1088  
1089 Buckley, S., Leverett, M., 1942. Mechanism of fluid displacement in sands.  
1090 Transactions of the American Institute of Mining 146, 107–116.
- 1091  
1092 Budek, A., Kwiatkiwski, K., Szymczak, P., 2017. Effect of mobility ratio  
1093 on interaction between teh fingers in unstable growth processes. *Physical  
1094 Review E* 96, 042218.
- 1095  
1096 Carvalho, G. D., Miranda, J. A., Gadêlha, H., Nov 2013. Interfacial elastic  
1097 fingering in Hele-Shaw cells: A weakly nonlinear study. *Phys. Rev. E* 88,  
1098 053006.
- 1099  
1100 Chang, Y., Pope, G., K.Seperhnoori, 1990. A higher-order finite difference  
1101 compositional simulator. *Journal of Petroleum Science and Engineering* 5,  
1102 35–50.
- 1103  
1104 Chavent, G., Jaffré, J., 1986. Mathematical Models and Finite Elements for  
1105 Reservoir Simulation. Vol. 17 of Studies in Mathematics and Its Applica-  
1106 tions. North Holland.
- 1107  
1108 Chen, Z., Huan, G., Ma, Y., 2006. Computational Methods for Multiphase  
1109 Flows in Porous Media. SIAM.
- 1110  
1111  
1112  
1113  
1114  
1115  
1116  
1117  
1118  
1119  
1120

- 1121  
1122  
1123  
1124  
1125  
1126  
1127  
1128 Chen, Z., Huan, G., Wang, H., 2005. Simulation of a compositional model  
1129 for multiphase flow in porous media. Numerical Methods for Partial Dif-  
1130 ferential Equations 21 (4), 726–741.  
1131  
1132 Cotter, C., Ham, D., C.C, P., Reich, S., 2009. LBB stability of a mixed  
1133 discontinuous/continuous galerkin finite element pair. Journal of Compu-  
1134 tational Physics 228, 336–348.  
1135  
1136 Courant, R., Friedrichs, K., Lewy, H., 1941. On difference equations of math-  
1137 ematical physics. Uspekhi Mat. Nauk 8, 125–160.  
1138  
1139 Cumming, B., 2012. Modelling sea water intrusion in coastal aquifers using  
1140 heterogeneous computing. Ph.D. thesis, Queensland University of Technol-  
1141 ogy, Australia.  
1142  
1143 Cumming, B., Moroney, T., Turner, I., 2011. A mass-conservative control  
1144 volume-finite element method for solving Richards' equation in heteroge-  
1145 neous porous media. BIT Numerical Mathematics 51 (4), 845–864.  
1146  
1147 Dawe, R., Grattoni, C., 2008. Experimental displacement patterns in a  $2 \times 3$   
1148 quadrant block with permeability and wettability heterogeneities problems  
1149 for numerical modelling. Transport in Porous Media 71, 5–22.  
1150  
1151 Evans, R., Dawe, R., 1994. The danger of neglecting nodal crossflow in het-  
1152 erogeneous near-wellbore conditions. Journal of Petroleum Science and En-  
1153 gineering 11 (2), 113–121.  
1154  
1155 Frey, P., George, P.-L., 2008. Mesh Generation, 2nd Edition. Wiley.  
1156  
1157 Fung, L., Hiebert, A., Nghiem, L., 1992. Reservoir simulation with control-  
1158 volume finite element method. SPE Reservoir Engineering 7 (3), 349–357.  
1159  
1160 Gomes, J., Pavlidis, D., Salinas, P., Percival, J., Xie, Z., Melnikova, Y.,  
1161 Pain, C., Jackson, M., 2017. A force balanced control volume finite el-  
1162 ement method for multi-phase porous media flow modelling. Int. J. Nu-  
1163 mer. Methods in Fluids 83, 431–455.  
1164  
1165 Gomes, J., Tollit, B., Milles, B., Pain, C., 2012. Fluidization Engineering –  
1166 Principles and Practice. National University of Singapore, Singapore, Ch.  
1167 Multi-Physics Flow Modelling for Nuclear Applications.  
1168  
1169  
1170

1171  
1172  
1173  
1174  
1175  
1176

- 1177  
1178  
1179  
1180  
1181  
1182  
1183  
1184 Guan, X., Pitchumani, R., 2003. Viscous fingering in a Hele-Shaw cell with  
1185 finite viscosity ratio and interfacial tension. *Transactions of the ASME* 125,  
1186 354–364.
- 1187  
1188 Habermann, B., 1960. The efficiency of miscible displacements as a function  
1189 of mobility ratio. *Petroleum Transactions, AIME* 219, 264–272.
- 1190  
1191 Hiester, H., Piggott, M., Farrell, P., Allison, P., 2014. Assessment of spurious  
1192 mixing in adaptive mesh simulations of the two-dimensional lock exchange.  
1193 *Ocean Modelling* 73, 30–44.
- 1194  
1195 Homsy, G., 1987. Viscous fingering in porous media. *Ann. Rev. Fluid Me-*  
1196 *chanics* 19, 271–311.
- 1197  
1198 Howison, S. D., 2000. A note on the two-phase Hele-Shaw problem. *Journal*  
1199 *of Fluid Mechanics* 409, 243–249.
- 1200  
1201 Jackson, M., Gomes, J., Mostaghimi, P., Percival, J., Tollit, B., Pavlidis,  
1202 D., Pain, C., El-Sheikh, A., Muggeridge, A., Blunt, M., 2013. Reservoir  
1203 modeling for flow simulation using surfaces, adaptive unstructured meshes,  
1204 and control-volume-finite-element methods. In: *SPE Reservoir Simulation*  
1205 *Symposium*.
- 1206  
1207 Jackson, M., Percival, J., Mostaghimi, P., Tollit, B., Pavlidis, D., Pain, C.,  
1208 Gomes, J., ElSheikh, A., Salinas, P., Muggeridge, A., Blunt, M., 2014. Reservoir  
1209 modeling for flow simulation by use of surfaces, adaptive unstruc-  
1210 tured meshes, and an overlapping-control-volume finite-element method.  
1211 *SPE Reservoir Evaluation & Engineering* 18 (2), SPE-163633-PA.
- 1212  
1213 Jackson, S., Power, H., Giddings, D., Stevens, D., 2017. The stability of  
1214 immiscible viscous fingering in Hele-Shaw cells with spatially varying per-  
1215 meability. *Computer Methods in Applied Mechanics and Engineering* 320,  
1216 606 – 632.
- 1217  
1218 Jiang, X., 2011. A review of physical modelling and numerical simulation of  
1219 long-term geological storage of carbon dioxide. *Applied Energy* 88, 3557–  
1220 3566.
- 1221  
1222 King, M., Mansfield, M., 1999. Flow simulation of geologic models. *SPE*  
1223 *Reservoir Evaluation & Engineering* SPE-57469-PA.
- 1224  
1225  
1226  
1227  
1228  
1229  
1230  
1231  
1232

- Kirkland, M., Hills, R., Wierenga, P., 1992. Algorithms for solving Richards' equation for variably-saturated soils. *Water Resources Research* 28, 2049–2058.
- Langtangen, H., Tveito, A., Winther, R., 1992. Instability of Buckley-Leverett flow in a heterogeneous medium. *Transport in Porous Media* 9, 165–185.
- Lo, S., 2015. Finite Element Mesh Generation. CRC Press.
- Lux, J., Anguy, Y., 2012. A study of the behavior of implicit pressure explicit saturation (IMPES) schedules for two-phase flow in dynamic pore network models. *Transp. Porous Med.* 93, 203–221.
- McLean, J., Saffman, P., 1981. The effect of surface tension on the shape of fingers in a Hele-Shaw cell. *J. Fluid Mechanics* 102, 455–469.
- Melnikova, Y., Jacquemyn, C., Osman, H., Salinas, P., Gorman, G., Hampson, G., Jackson, M., 2016. Reservoir modelling using parametric surfaces and dynamically adaptive fully unstructured grids. In: Proceedings of the XV European Conference on the Mathematics of Oil Recovery (ECMOR XV). EAGE.
- Mlacnik, M., Durlofsky, L., Heinemann, Z., 2004. Dynamic flow-based PEBI grids for reservoir simulation. SPE 90009.
- Mostaghimi, P., Kamall, F., Jackson, M., Muggeridge, A., Pain, C., 2016. Adaptive mesh optimisation for simulation of immiscible viscous fingering. *SPE Journal* 21, 250–259.
- Muskat, M., 1934. Two fluid systems in porous media. the encroachment of water into an oil sand. *Journal of Applied Physics* 5, 250–264.
- Nick, H., Matthai, S., 2011a. Comparison of three FE-FV numerical schemes for single- and tw-phase flow simulation of fractured porous media. *Transp. Porous Med* 90, 421–444.
- Nick, H., Matthai, S., 2011b. A hybrid finite-element finite-volume method with embedded discontinuities for solute transport in heterogeneous media. *Vadose Zone Journal* 10, 299–312.

- 1289  
1290  
1291  
1292  
1293  
1294  
1295  
1296 Nicolaides, C., Jha, B., Cueto-Felgueroso, L., Juanes, R., 2015. Impact of  
1297 viscous fingering and permeability heterogeneity on fluid mixing porous  
1298 media. *Water Resources Research* 51, WR015811.
- 1299  
1300 Pain, C., Umpleby, A., de Oliveira, C., Goddard, A., 2001. Tetrahedral mesh  
1301 optimisation and adaptivity for steady-state and transient finite element  
1302 calculations. *Computer Methods in Applied Mechanics and Engineering*  
1303 190, 3771–3796.
- 1304  
1305 Paluszny, A., Matthai, S., Hohmeyer, M., 2007. Hybrid finite element finite  
1306 column discretization of complex geologic structures and a new simulation  
1307 workflow demonstrated on fractured rocks. *Geofluids* 7, 186–208.
- 1308  
1309 Pavlidis, D., Gomes, J., Xie, Z., Percival, J., Pain, C., Matar, O., 2016. Com-  
1310 pressive advection and multi-component methods for interface-capturing.  
1311 *International Journal for Numerical Methods in Fluids* 80 (4), 256–282.
- 1312  
1313 Pietro, D. D., Vohralík, M., Yousef, S., 2014. An a posteriori-based, fully  
1314 adaptive algorithm with adaptive stopping criteria and mesh refinement  
1315 for thermal multiphase compositional flows in porous media. *Computers  
1316 and Mathematics with Applications* 68 (12B), 2331–2347.
- 1317  
1318 Piggott, M., Pain, C., Gorman, G., Power, P., Goddard, A., 2006. h,r and hr  
1319 adaptivity with application in numerical ocean modelling. *Ocean Modelling*  
1320 10, 95–113.
- 1321  
1322 Plewa, T., Linde, T., Weirs, V. (Eds.), 2004. Adaptive Mesh Refinement  
1323 – Theory and Applications. Vol. 41 of *Lecture Notes in Computational  
1324 Science and Engineering*. Springer.
- 1325  
1326 Power, P., Piggott, M., Fang, F., Gorman, G., Pain, C., Marshall, D., God-  
1327 dard, A., 2006. Adjoint goal-based error norms for adaptive mesh ocean  
1328 modelling. *Ocean Modelling* 15, 3–38.
- 1329  
1330 Praud, O., Swinney, H. L., Jul 2005. Fractal dimension and unscreened angles  
1331 measured for radial viscous fingering. *Phys. Rev. E* 72, 011406.
- 1332  
1333 Radünz, W., Oliveira, F., Gomes, J., July 2014. A multi-scale model of  
1334 multi-fluid flows transport in dual saturated-unsaturated heterogeneous  
1335  
1336  
1337  
1338

- 1345  
1346  
1347  
1348  
1349  
1350  
1351  
1352 porous media. In: Onate, E., Oliver, J., Huerta, A. (Eds.), Proceedings of the XI World Congress on Computational Mechanics (WCCM XI).  
1353 IACM/ECCOMAS, Barcelona, Spain.  
1354  
1355  
1356 Riaz, A., Tchelepi, H. A., 2004. Linear stability analysis of immiscible two-  
1357 phase flow in porous media with capillary dispersion and density variation.  
1358 Physics of Fluids 16 (12), 4727–4737.  
1359  
1360 Saffman, P., 1959. Theory of dispersion in porous medium. J. Fluid Mechanics  
1361 6, 321–349.  
1362  
1363 Saffman, P., 1986. Viscous fingering in Hele-Shaw cells. J. Fluid Mechanics  
1364 173, 73–94.  
1365  
1366 Saffman, P., Taylor, G. I., 1958. The penetration of a fluid into a porous  
1367 medium or Hele-Shaw cell containing a more viscous liquid. Proc. R. Soc.  
1368 London A 245, 321–329.  
1369  
1370 Salinas, P., Pavlidis, D., Xie, Z., Adam, A., Pain, C., Jackson, M., 2016. Im-  
1371 proving the convergence behaviour of a fixed-point-iteration solver for mul-  
1372 tiphase flow in porous media. International Journal for Numerical Methods  
1373 in Fluids 84, 466–476.  
1374  
1375 Salinas, P., Pavlidis, D., Xie, Z., Osman, H., Pain, C., Jackson, M., 2018.  
1376 A discontinuous control volume finite element method for multiphase flow  
1377 in heterogeneous porous media. Journal of Computational Physics 352,  
1378 602–614.  
1379  
1380 Salinas, P., Percival, J., Pavlidis, D., Xie, Z., Gomes, J., Pain, C., Jackson,  
1381 M., et al., 2015. A discontinuous overlapping control volume finite element  
1382 method for multi-phase porous media flow using dynamic unstructured  
1383 mesh optimization. In: SPE-173279-MS, Reservoir Simulation Symposium.  
1384 Society of Petroleum Engineers.  
1385  
1386 Self, S., Reddy, B., Rosen, M., 2012. Review of underground coal gasifica-  
1387 tion technologies and carbon capture. International Journal of Energy and  
1388 Environmental Engineering 3, 16–24.  
1389  
1390 Sheldon, J., Cardwell, W., 1959. One-dimensional, incompressible, noncapil-  
1391 lary two-phase fluid flow in a porous media. Petroleum Transactions, AIME  
1392 216.  
1393  
1394

1345  
1346  
1347  
1348  
1349  
1350  
1351  
1352  
1353  
1354  
1355  
1356  
1357  
1358  
1359  
1360  
1361  
1362  
1363  
1364  
1365  
1366  
1367  
1368  
1369  
1370  
1371  
1372  
1373  
1374  
1375  
1376  
1377  
1378  
1379  
1380  
1381  
1382  
1383  
1384  
1385  
1386  
1387  
1388  
1389  
1390  
1391  
1392  
1393  
1394  
1395  
1396  
1397  
1398  
1399  
1400

- 1401  
1402  
1403  
1404  
1405  
1406  
1407  
1408 Spycher, N., Pruess, K., Ennis-King, J., 2003. CO<sub>2</sub>-H<sub>2</sub>O mixtures in the  
1409 geological sequestration of CO<sub>2</sub>. II. Assessment and calculation of mutual  
1410 solubilities from 12 to 100°C and up to 600 bar. *Geochim. Cosmochim.*  
1411 *Acta* 67 (16), 2015–3031.  
1412  
1413 Su, K., Latham, J., Pavlidis, D., Xiang, J., Fang, F., Mostaghimi, P., Per-  
1414 cival, J., Pain, C., Jackson, M., 2016. Multiphase flow simulation through  
1415 porous media with explicitly resolved fractures. *Geofluids* 15, 592–607.  
1416  
1417 Tabeling, P., Zocchi, G., Libchaber, A., 1987. An experimental study of the  
1418 Saffman-Taylor instability. *Journal of Fluid Mechanics* 177, 67–82.  
1419  
1420 Tan, C., Homsy, G., 1988. Simulation of nonlinear viscous fingering in mis-  
1421 cible displacement. *Physics of Fluids* 31, 1330–1338.  
1422  
1423 Tavassoli, S., Pope, G. A., Sepehrnoori, K., et al., 2015. Frontal-stability  
1424 analysis of surfactant floods. *SPE Journal* 20 (03), 471–482.  
1425  
1426 Tchelepi, H., Jr, F. O., 1994. Interaction of viscous fingering, permeability  
1427 heterogeneity and gravity segregation in three dimensions. *SPE* 25235,  
1428 266–271.  
1429  
1430 Voller, V., 2009. Basic Control Volume Finite Element Methods for Fluids  
1431 and Solids. Vol. 1 of IISc Research Monographs Series. World Scientific  
1432 Publishing Co, Singapore.  
1433  
1434 White, I., Lewis, R., W, L, W., 1981. The numerical simulation of multiphase  
1435 flow through a porous medium and its application to reservoir engineering.  
1436 *Applied Mathematical Modelling* 5, 165–172.  
1437  
1438 Wing, R., Russel, T., Young, L., 1989. An anisotropic coarse-grid disper-  
1439 sion model of heterogeneity and viscous fingering in five-spot miscible  
1440 displacement that matches experiments and fine-grid simulations. *SPE* 18441,  
1441 447–465.  
1442  
1443 Wooding, R. A., Morel-Seytoux, 1976. Multiphase fluid flow through porous  
1444 media. *Ann. Rev. Fluid Mechanics* 8, 233–274.  
1445  
1446  
1447  
1448  
1449  
1450  
1451  
1452  
1453  
1454  
1455  
1456

1457  
1458  
1459  
1460  
1461  
1462  
1463  
1464

## List of Tables

- 1465  
1466  
1467  
1468  
1469  
1470  
1471  
1472  
1473  
1474  
1475  
1476  
1477  
1478  
1479  
1480  
1481  
1482  
1483  
1484  
1485  
1486  
1487  
1488  
1489  
1490  
1491  
1492  
1493  
1494  
1495  
1496  
1497  
1498  
1499  
1500  
1501  
1502  
1503  
1504  
1505  
1506  
1507  
1508  
1509  
1510  
1511  
1512
- |   |                                                                                                                                                                                                                                                                                                                                             |    |
|---|---------------------------------------------------------------------------------------------------------------------------------------------------------------------------------------------------------------------------------------------------------------------------------------------------------------------------------------------|----|
| 1 | Sumary of model set-up used in the numerical simulations.<br>Superscript $\circ$ denotes initial condition. $\mathbf{K}_i$ is in $cm^2$ and $u_w^\circ$<br>is in m/sec. $S_{w,irr}$ and $S_{nw,r}$ are the same for all simulations.                                                                                                        | 28 |
| 2 | Flow simulations in Heleshaw cells (Section 4.3): summary of<br>finger width calculations using Eqn. 10 and obtained through<br>numerical simualtions. $\lambda_f^{calc}$ was calculated based on fingers'<br>tip velocities and outflow rate. Calculations were based on<br>simulation data obtained from snapshots shown in Fig. 8. . . . | 29 |

<b>Section</b>	$\phi$	VR	$S_w^0$	$S_{nw}^0$	$\mathbf{K}_1$	$\mathbf{K}_2$	$\mathbf{K}_3$	$\mathbf{K}_4$	$S_{w,irr}$	$S_{nw,r}$	$u_w^\circ$
<b>4.2</b>	0.2	1.0	0.0	1.0	2.5	1.0	N/A	N/A	0.2	0.3	1.0
<b>4.3(homogenous)</b>	0.2	10.0	0.0	1.0	1.e-10	N/A	N/A	N/A	0.2	0.3	0.5
<b>4.3(heterogenous)</b>	0.2	1.0	0.0	1.0	1.e-11 – 5.e-10	1.e-12 – 5.e-10	1.e-12 – 1.e-10	1.e-10	0.2	0.3	1.0
<b>4.4</b>	0.2	1.0	0.0	1.0	3.0	2.0	5.0	1.0	0.2	0.3	0.5
<b>4.5</b>	0.2	1.0	0.0	1.0	3.0	2.0	5.0	1.0	0.2	0.3	0.5

Table 1: Sumary of model set-up used in the numerical simulations. Superscript  $\circ$  denotes initial condition.  $\mathbf{K}_i$  is in  $cm^2$  and  $u_w^\circ$  is in m/sec.  $S_{w,irr}$  and  $S_{nw,r}$  are the same for all simulations.

	<b>K</b> (cm <sup>2</sup> )	<i>VR</i>	$\lambda_f^{(\text{calc,max})}$ (cm) (Eqn. 10)	$\lambda_f^{(\text{simul,max})}$ (cm)
<b>Case 1</b> (homogeneous)	$1 \times 10^{-10}$	10	0.13-0.75	0.45-0.70
<b>Case 2</b> (homogeneous)	$1 \times 10^{-10}$	150	0.30-0.75	0.50-0.90
<b>Case 3</b> (heterogeneous)	$1 \times 10^{-12}$ - $5 \times 10^{-10}$	10	0.25-4.50	0.44-0.56
<b>Case 4</b> (heterogeneous)	$1 \times 10^{-12}$ - $5 \times 10^{-10}$	150	0.88-3.00	0.24-0.40

Table 2: Flow simulations in Heleshaw cells (Section 4.3): summary of finger width calculations using Eqn. 10 and obtained through numerical simulations.  $\lambda_f^{\text{calc}}$  was calculated based on fingers' tip velocities and outflow rate. Calculations were based on simulation data obtained from snapshots shown in Fig. 8.

1597  
 1598  
 1599  
 1600  
 1601  
 1602  
 1603  
 1604

## List of Figures

1605	1	2D representation of P <sub>1</sub> DG-P <sub>2</sub> element pairs used in this work. Shaded areas denote control volumes across two contiguous elements. Blue and white circles represent pressure and velocity nodes, respectively. . . . .	33
1606	2	This is a graphical representation of two different element types. Triangle <i>A</i> is a representation of the P <sub>1</sub> DG-P <sub>2</sub> element-pair, whereas triangle <i>B</i> represents the P <sub>1</sub> DG-P <sub>1</sub> element-pair. Porosity $\phi_i$ , permeability $\mathbf{K}_i$ , velocity and pressure are primarily represented in FE space whereas scalar fields (such as saturation, density, viscosity etc) are represented in CV space. . . . .	34
1607	3	Schematics of formation of flow instabilities during injection of a pure low viscosity fluid (red) into a domain saturated with a second fluid (dark blue). The viscosity ratio of the two fluids is VR=5. In this case, the initially piston shape front collapses leading to the formation of several fingers. . . . .	35
1608	4	Model validation of fluid displacement in heterogeneous porous media (VR=1): (a) the domain is divided into four subdomains with prescribed synthetic permeability, $K_1 = 1$ and $K_2 = 2.5$ ; (b-c) snapshots of saturation (displacing fluid) field at t=25 and t=300. The domain is discretised with 5960 P <sub>1</sub> DG-P <sub>2</sub> elements. . . . .	36
1609	5	Simulated flow in a Hele-Shaw cell (VR=3, $K=10^{-10}\text{cm}^2$ ): (a) initial pressure profile (in $\text{g.cm}^{-1}.\text{s}^{-2}$ ) with source and sink regions explicitly shown along with dimensions (in cm); (b-f) snapshots of wetting phase saturation showing flow profile as the simulation evolves. The domain contains 26313 P <sub>1</sub> DG-P <sub>2</sub> triangular elements. . . . .	37
1610	6	Simulated flow in a Hele-Shaw cell (VR=10, $K=10^{-10}\text{cm}^2$ ): snapshots of overlapped wetting phase saturation and velocity vectors showing flow profile as the simulation evolves. The domain contains 26313 P <sub>1</sub> DG-P <sub>2</sub> triangular elements. . . . .	38
1611	7	Simulated flow in a Hele-Shaw cell (VR=150, $K=10^{-10}\text{cm}^2$ ): snapshots of wetting phase saturation showing flow profile as the simulation evolves. The domain contains 26313 P <sub>1</sub> DG-P <sub>2</sub> triangular elements. . . . .	39

- 1653  
 1654  
 1655  
 1656  
 1657  
 1658  
 1659  
 1660 8 Isosurfaces of simulated flows in Hele-Shaw cells with viscos-  
 1661 ity ratios of 10 (a and c) and 150 (b and d). Top and bottom  
 1662 rows describe simulations performed with constant *i.e.* *homoge-*  
 1663 *neous* with  $K = 10^{-10} \text{ cm}^2$  and randomly distributed (*i.e.*  
 1664 heterogeneous, Fig. 9a) permeabilities. Width of largest fin-  
 1665 gers for homogeneous cases are approximately 0.70 and 0.90cm  
 1666 ( $VR=10$  and  $VR=150$ , respectively), whereas for heteroge-  
 1667 neous cases are 0.56 and 0.40cm. Results for homogeneous  
 1668 cases are in good agreement with values obtained from Guan  
 1669 and Pitchumani (2003)'s analytic solution. . . . . 40  
 1670  
 1671 9 Simulated flow in a modified Hele-Shaw cell with  $VR=10$ : (a)  
 1672 permeability distribution ( $10^{-10} \leq K_1 \leq 5 \times 10^{-10}$ ,  $K_2=10^{-10}$ ,  
 1673  $10^{-11} \leq K_3 \leq 5 \times 10^{-10}$  and  $10^{-12} \leq K_4 \leq 5 \times 10^{-10} \text{ cm}^2$ );  
 1674 (b-f) snapshots of saturation profile during 9.77 seconds of  
 1675 simulation. The domain contains 26313 P<sub>1</sub>DG-P<sub>2</sub> element-pairs. 41  
 1676  
 1677 10 Simulated flow in a modified Hele-Shaw cell with  $VR=150$ :  
 1678 snapshots of saturation profile during 2.50 seconds of sim-  
 1679 ulation. Permeability distribution used in this simulation was  
 1680 the same as shown in Fig. 9a. The domain contains 26313  
 1681 P<sub>1</sub>DG-P<sub>2</sub> element-pairs. . . . . 42  
 1682  
 1683 11 Simulated flow in a modified Hele-Shaw cell with  $VR=150$ :  
 1684 snapshots of saturation profile. Permeability distribution used  
 1685 in this simulation was the same as shown in Fig. 9a. The  
 1686 domain contains 3734 P<sub>1</sub>DG-P<sub>2</sub> element-pairs. . . . . 43  
 1687  
 1688 12 Impact of mesh resolution on capturing flow instabilities: (a)  
 1689 permeability and (b) initial saturation and mesh resolution  
 1690 used in the simulations performed in Section 4.4. There are  
 1691 13068 P<sub>1</sub>DG-P<sub>2</sub> element-pairs in the domain. . . . . 44  
 1692  
 1693 13 Impact of mesh resolution on capturing flow instabilities: snap-  
 1694 shots of saturation field through 1.50 seconds of numerical  
 1695 simulation performed with fixed mesh (of 13068 elements) and  
 1696  $VR=10$ . . . . . 45  
 1697  
 1698 14 Impact of mesh resolution on capturing flow instabilities: snap-  
 1699 shots of saturation field through 1.50 seconds of numerical  
 1700 simulation performed with adaptive mesh and  $VR=10$ . . . . . 46  
 1701 15 Impact of mesh resolution on capturing flow instabilities: total  
 1702 number of elements and nodes for simulations performed with  
 1703 fixed and adaptive mesh. . . . . 47  
 1704  
 1705  
 1706  
 1707  
 1708

1709		
1710		
1711		
1712		
1713		
1714		
1715		
1716	16 Impact of mesh resolution on flow instabilities: capturing for-	
1717	matation and growth of flow instabilities at fluid interfaces ( $t$	
1718	= 0.20 s) in two regions of the computational domain, $A$ and	
1719	$B$ . Simulations were conducted with fixed (left-hand side) and	
1720	adaptive meshes. . . . .	48
1721	17 3D channel flow (fixed mesh): permeability distribution. The	
1722	domain contains 243056 $P_1$ DG- $P_1$ element-pairs. . . . .	49
1723	18 3D channel flow (fixed mesh): XY and YZ planes showing	
1724	wetting fluid phase Darcy velocity vectors overlapped with	
1725	wetting fluid saturation at (a) $t=0.29s$ and (b) $t=4.3s$ . . . . .	50
1726	19 3D channel flow (fixed mesh): saturation front evolving in	
1727	time and space with preferential flow pathways through 3.50	
1728	seconds of numerical simulations. Preferential flow pathway	
1729	can be readily noticed in these frames, mirroring permeability	
1730	distribution. The domain contains 368513 $P_1$ DG- $P_1$ elements.	51
1731	20 3D channel flow (fixed mesh): Isosurfaces for wetted phase	
1732	saturatioh ranging from 0.45 and 0.60 at the same instants	
1733	of time of Fig. 19. Preferential flow pathway can be readily	
1734	noticed in (b) and (f). Fingers' formation and growth can be	
1735	clearly noticed in (b)-(e). The domain contains 368513 $P_1$ DG-	
1736	$P_1$ elements. . . . .	52
1737	21 3D channel flow (adaptive mesh): numerical simulation was	
1738	performed with the smae boundary and initial conditions as	
1739	in Figs. 17-20 with an adaptive mesh. Flow pathway is very	
1740	similar to the one shown in Fig. 19. . . . .	53
1741	22 3D Channel (adaptive mesh): XY and YZ planes showing wet-	
1742	ting fluid saturation overlapped with Darcy velocity vectors	
1743	at (a) 0.00, (b) 0.09, (c) 0.71, (d) 1.75, (e) 2.47 and (f) 3.78s.	
1744	Colour scheme for saturation profile is the same as used in	
1745	Fig. 21. . . . .	54
1746	23 3D Channel: Text to come . . . . .	55
1747		
1748		
1749		
1750		
1751		
1752		
1753		
1754		
1755		
1756		
1757		
1758		
1759		
1760		
1761		
1762		
1763		
1764		

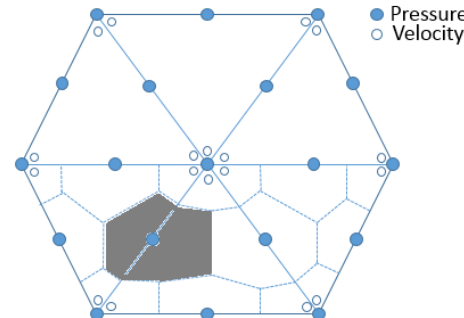


Figure 1: 2D representation of  $P_1$ DG- $P_2$  element pairs used in this work. Shaded areas denote control volumes across two contiguous elements. Blue and white circles represent pressure and velocity nodes, respectively.

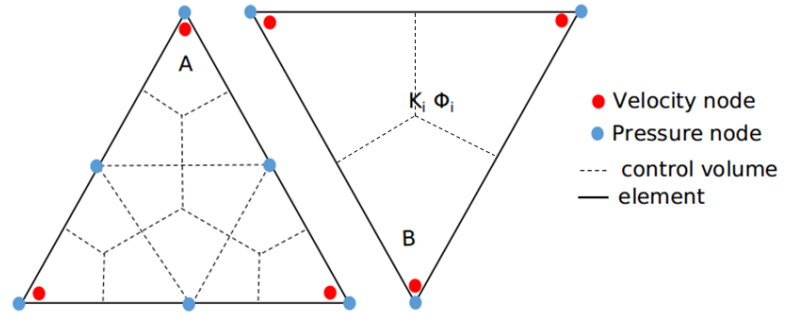


Figure 2: This is a graphical representation of two different element types. Triangle  $A$  is a representation of the  $P_1$ DG- $P_2$  element-pair, whereas triangle  $B$  represents the  $P_1$ DG- $P_1$  element-pair. Porosity  $\phi_i$ , permeability  $\mathbf{K}_i$ , velocity and pressure are primarily represented in FE space whereas scalar fields (such as saturation, density, viscosity etc) are represented in CV space.

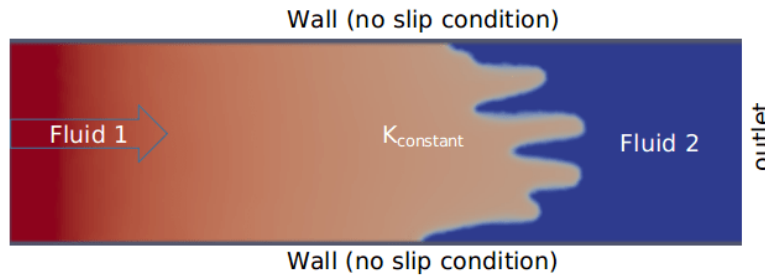
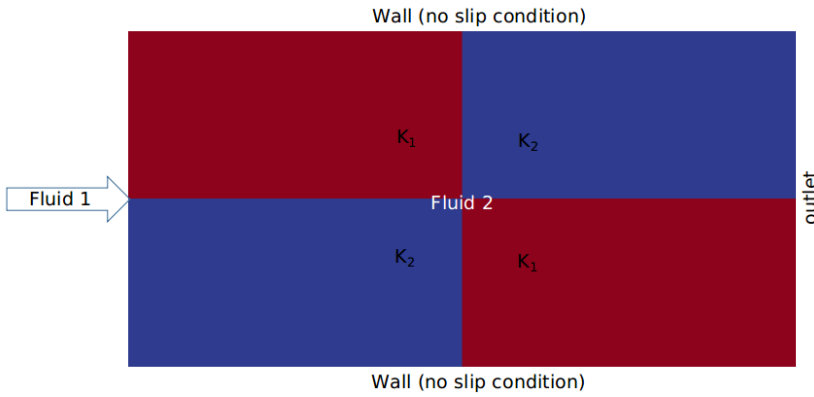
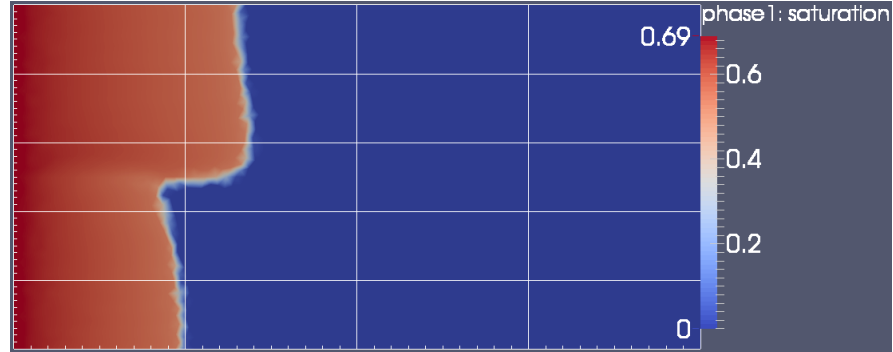


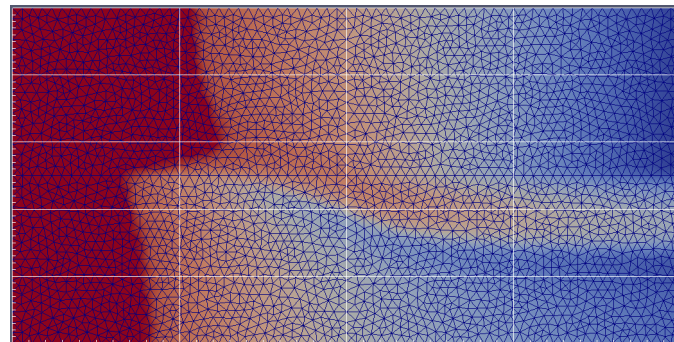
Figure 3: Schematics of formation of flow instabilities during injection of a pure low viscosity fluid (red) into a domain saturated with a second fluid (dark blue). The viscosity ratio of the two fluids is  $VR=5$ . In this case, the initially piston shape front collapses leading to the formation of several fingers.



1951  
1952 (a) Schematics of the domain with permeability ( $\mathbf{K}$ ) distribution



1964 (b) flow at  $t=25$



1976 (c) flow at  $t=3000$

1977 Figure 4: Model validation of fluid displacement in heterogeneous porous media ( $VR=1$ ):  
1978 (a) the domain is divided into four subdomains with prescribed synthetic permeability,  
1979  $\mathbf{K}_1 = 1$  and  $\mathbf{K}_2 = 2.5$ ; (b-c) snapshots of saturation (displacing fluid) field at  $t=25$  and  
1980  $t=300$ . The domain is discretised with 5960  $P_1$ DG- $P_2$  elements.

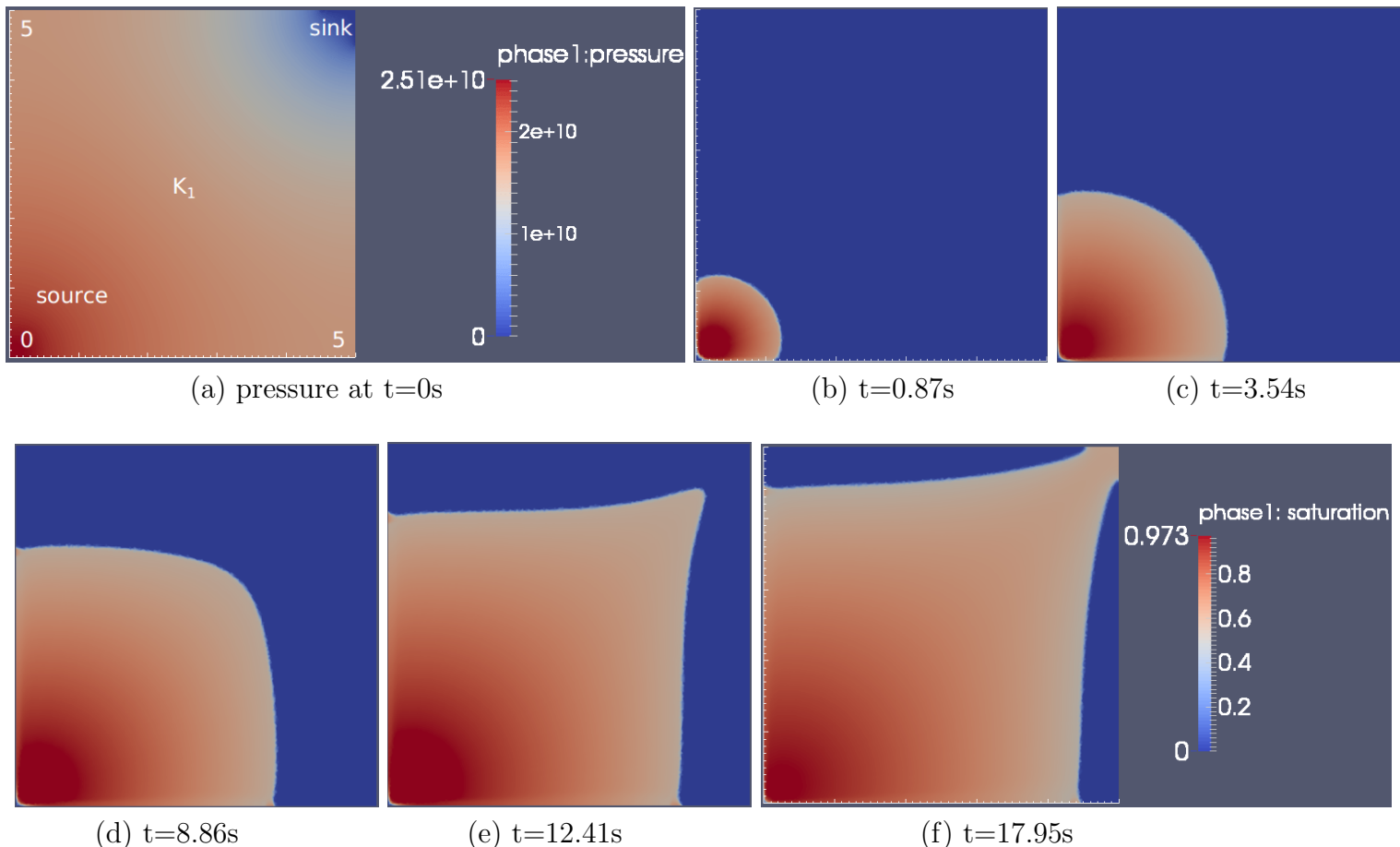


Figure 5: Simulated flow in a Hele-Shaw cell ( $VR=3$ ,  $\mathbf{K}=10^{-10}\text{cm}^2$ ): (a) initial pressure profile (in  $\text{g.cm}^{-1}.\text{s}^{-2}$ ) with source and sink regions explicitly shown along with dimensions (in cm); (b-f) snapshots of wetting phase saturation showing flow profile as the simulation evolves. The domain contains 26313  $P_1$ DG- $P_2$  triangular elements.

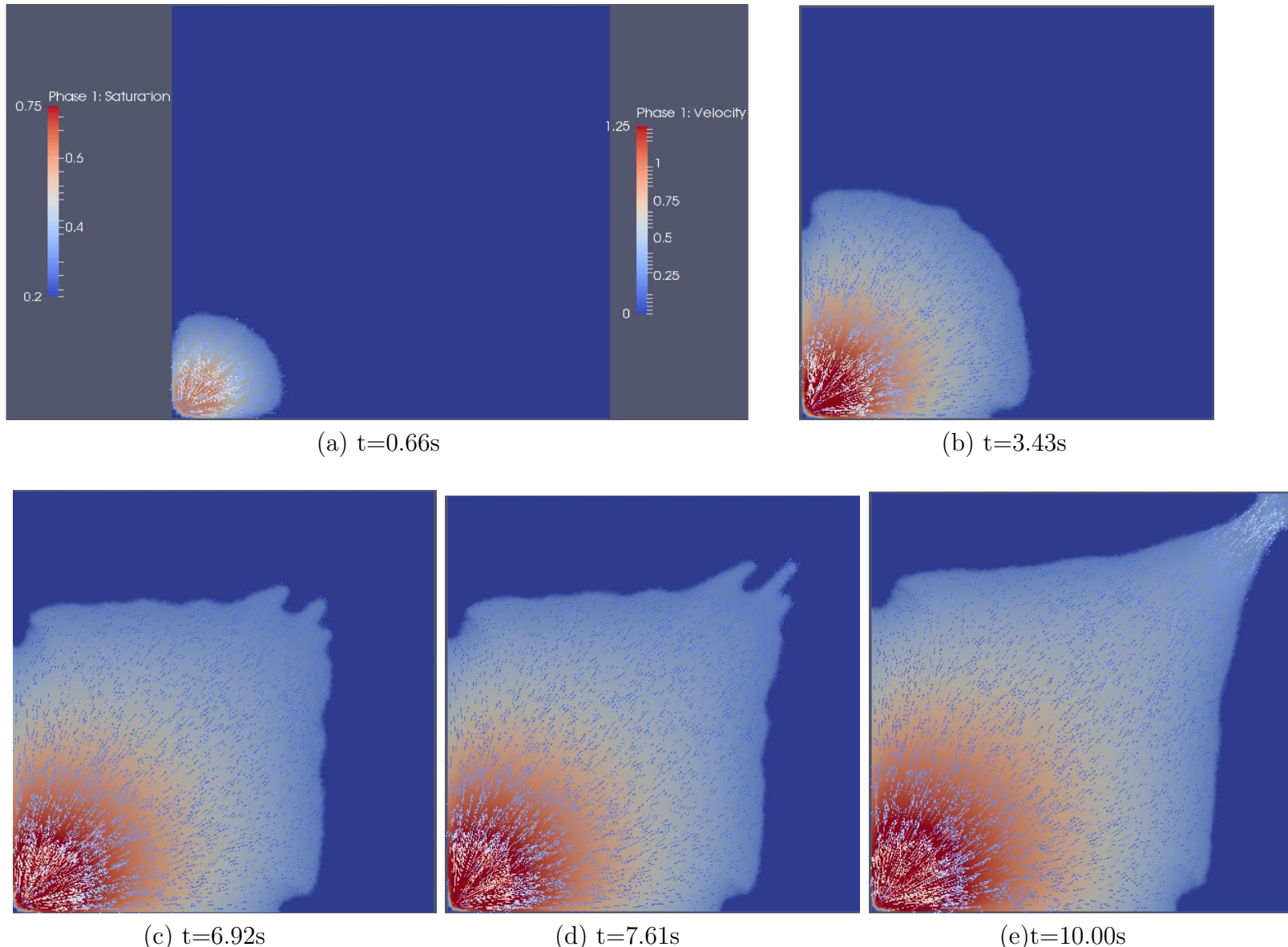


Figure 6: Simulated flow in a Hele-Shaw cell ( $VR=10$ ,  $\mathbf{K}=10^{-10}\text{cm}^2$ ): snapshots of overlapped wetting phase saturation and velocity vectors showing flow profile as the simulation evolves. The domain contains 26313  $P_1$ DG- $P_2$  triangular elements.

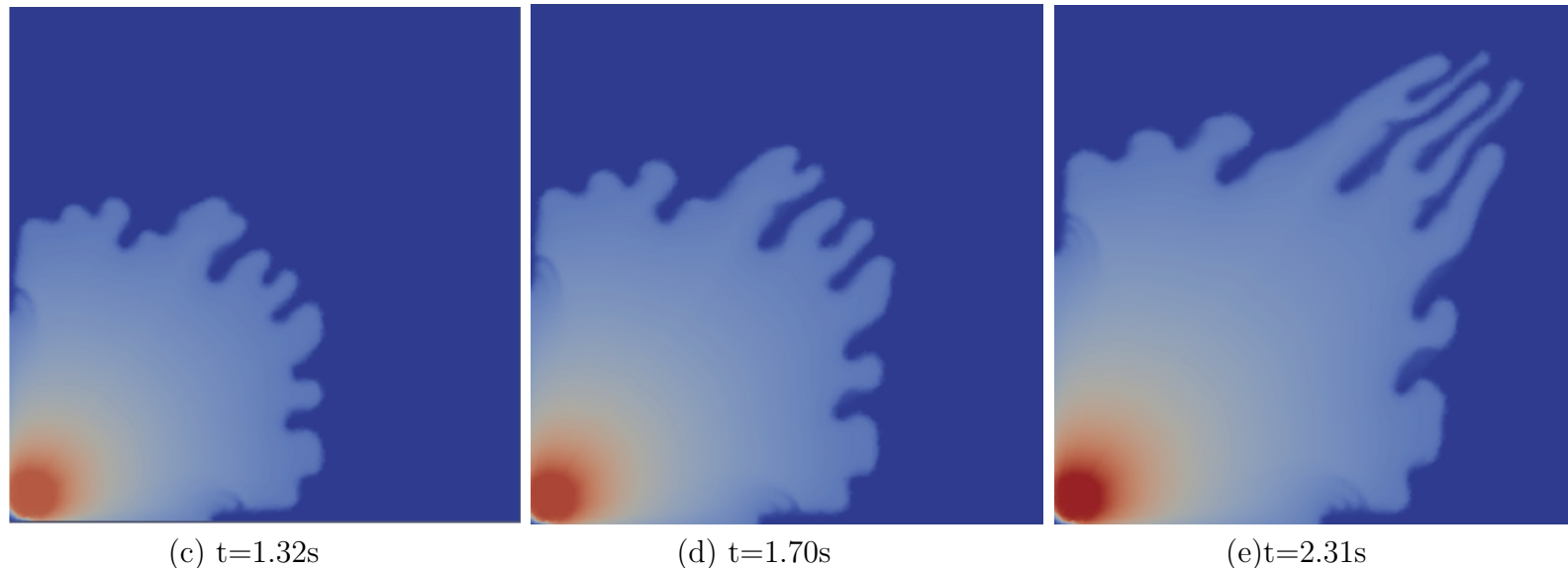
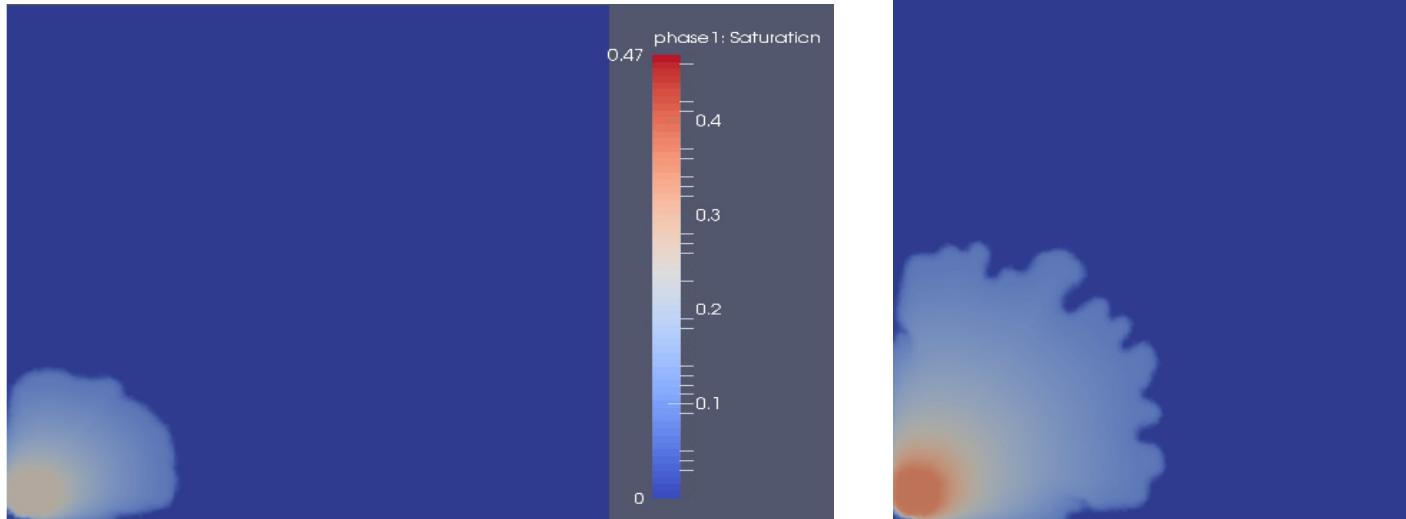


Figure 7: Simulated flow in a Hele-Shaw cell ( $VR=150$ ,  $\mathbf{K}=10^{-10}\text{cm}^2$ ): snapshots of wetting phase saturation showing flow profile as the simulation evolves. The domain contains 26313  $P_1\text{DG}-P_2$  triangular elements.

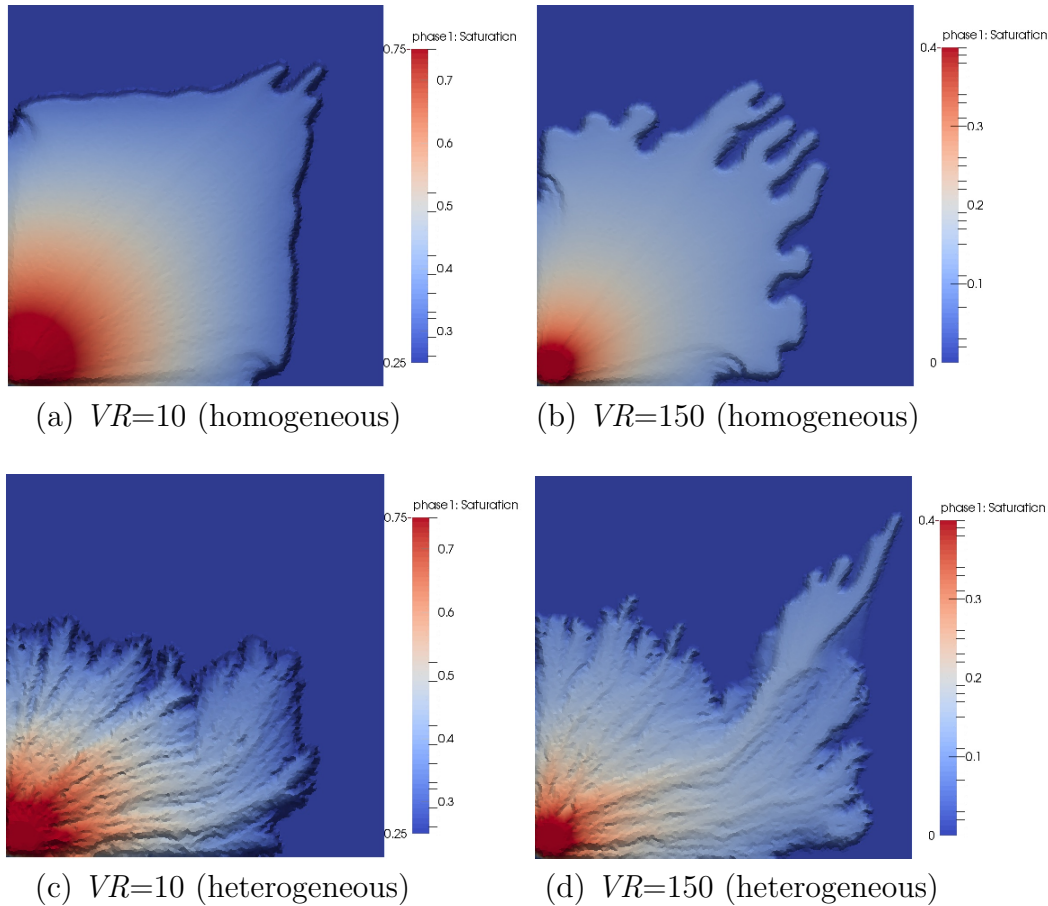


Figure 8: Isosurfaces of simulated flows in Hele-Shaw cells with viscosity ratios of 10 (a and c) and 150 (b and d). Top and bottom rows describe simulations performed with constant *i.e. homogeneous with  $K = 10^{-10} \text{ cm}^2$*  and randomly distributed (*i.e. heterogeneous, Fig. 9a*) permeabilities. Width of largest fingers for homogeneous cases are approximately 0.70 and 0.90cm ( $VR=10$  and  $VR=150$ , respectively), whereas for heterogeneous cases are 0.56 and 0.40cm. Results for homogeneous cases are in good agreement with values obtained from [Guan and Pitchumani \(2003\)](#)'s analytic solution.

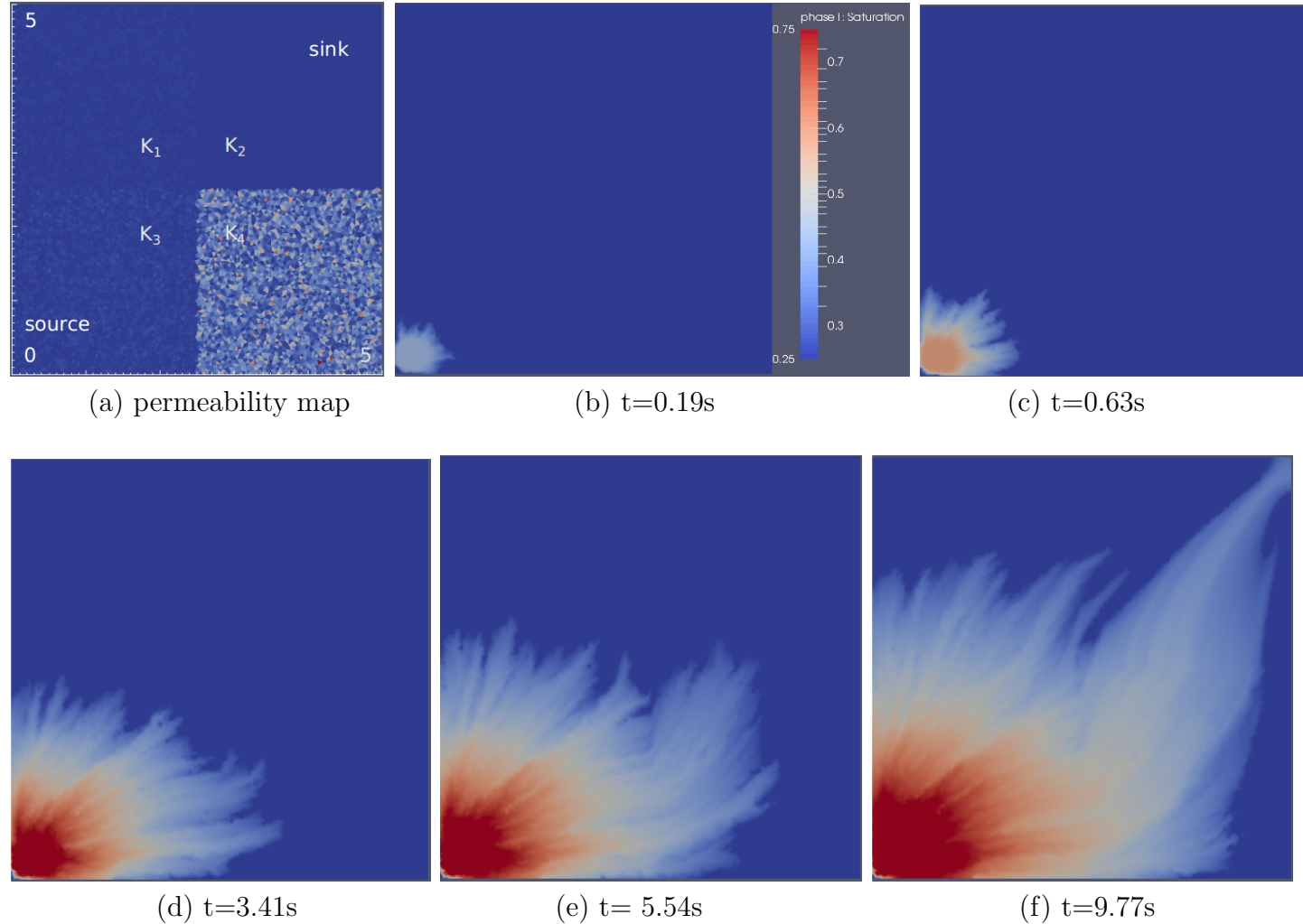
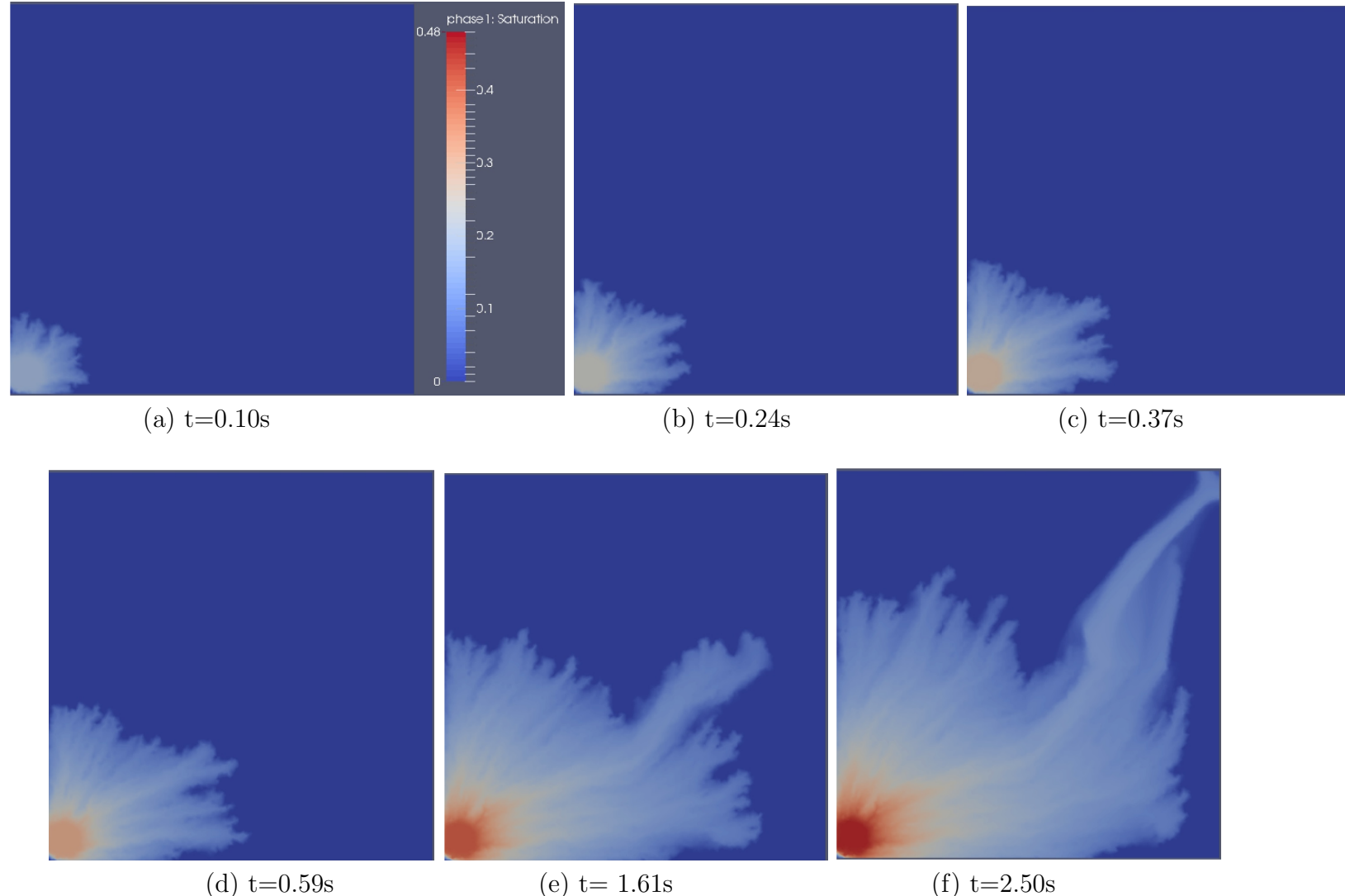


Figure 9: Simulated flow in a modified Hele-Shaw cell with  $VR=10$ : (a) permeability distribution ( $10^{-10} \leq \mathbf{K}_1 \leq 5 \times 10^{-10}$ ,  $\mathbf{K}_2=10^{-10}$ ,  $10^{-11} \leq \mathbf{K}_3 \leq 5 \times 10^{-10}$  and  $10^{-12} \leq \mathbf{K}_4 \leq 5 \times 10^{-10} \text{ cm}^2$ ); (b-f) snapshots of saturation profile during 9.77 seconds of simulation. The domain contains 26313 P<sub>1</sub>DG-P<sub>2</sub> element-pairs.



2250  
 2251  
 2252  
 2253  
 2254

Figure 10: Simulated flow in a modified Hele-Shaw cell with  $VR=150$ : snapshots of saturation profile during 2.50 seconds of simulation. Permeability distribution used in this simulation was the same as shown in Fig. 9a. The domain contains 26313  $P_1$ DG- $P_2$  element-pairs.

2255  
2256  
2257  
2258  
2259  
2260  
2261  
2262  
2263  
2264  
2265  
2266  
2267  
2268  
2269  
2270  
2271  
2272

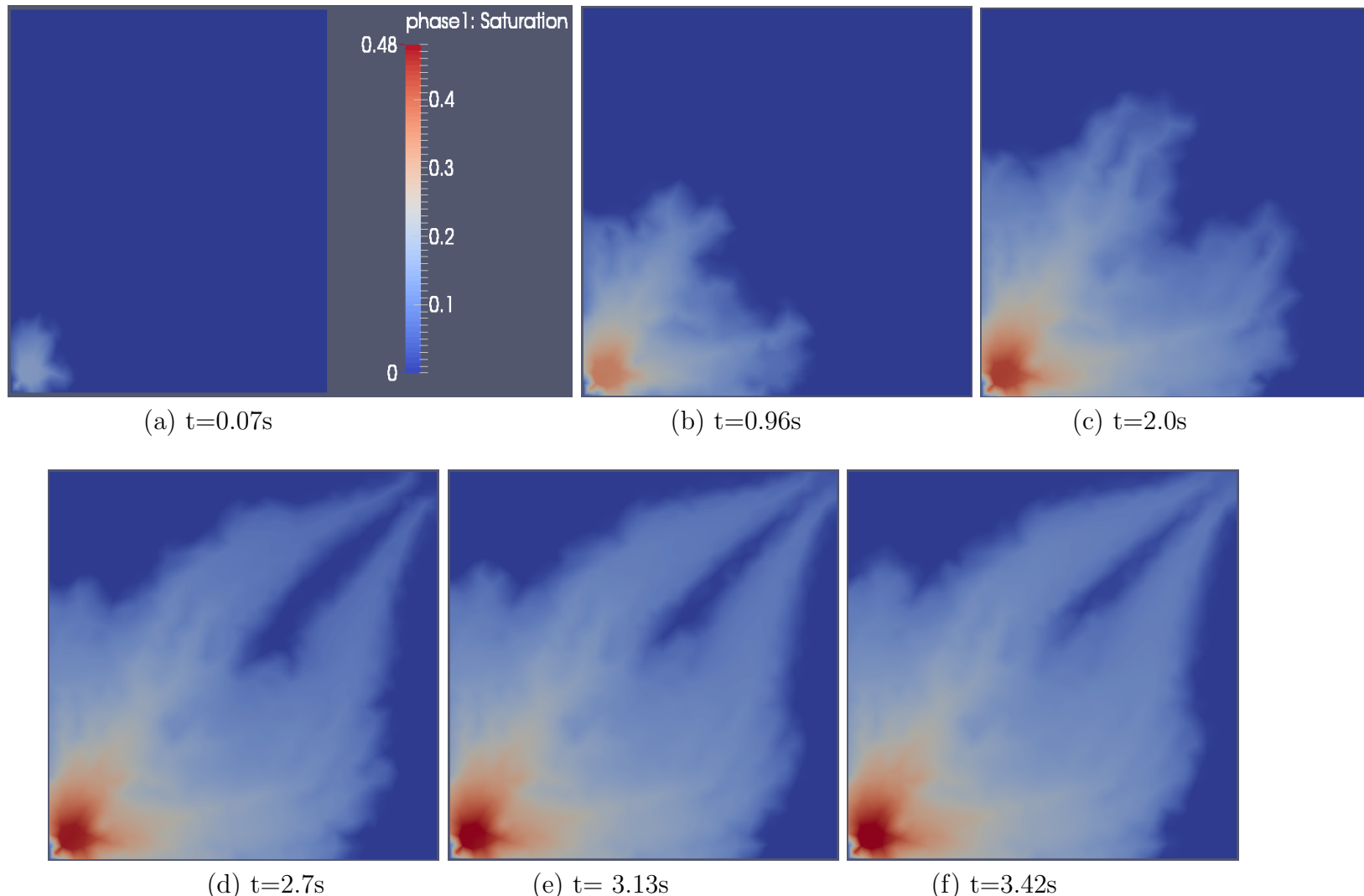
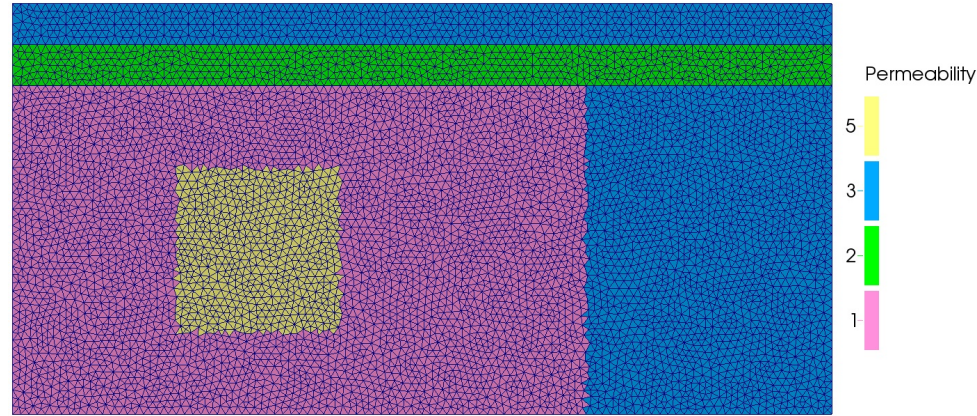


Figure 11: Simulated flow in a modified Hele-Shaw cell with  $VR=150$ : snapshots of saturation profile. Permeability distribution used in this simulation was the same as shown in Fig. 9a. The domain contains 3734  $P_1$ DG- $P_2$  element-pairs.



(a) Permeability mapping ( $\mathbf{K}$ )



(b) Initial saturation distribution

Figure 12: Impact of mesh resolution on capturing flow instabilities: (a) permeability and (b) initial saturation and mesh resolution used in the simulations performed in Section 4.4. There are 13068 P<sub>1</sub>DG-P<sub>2</sub> element-pairs in the domain.

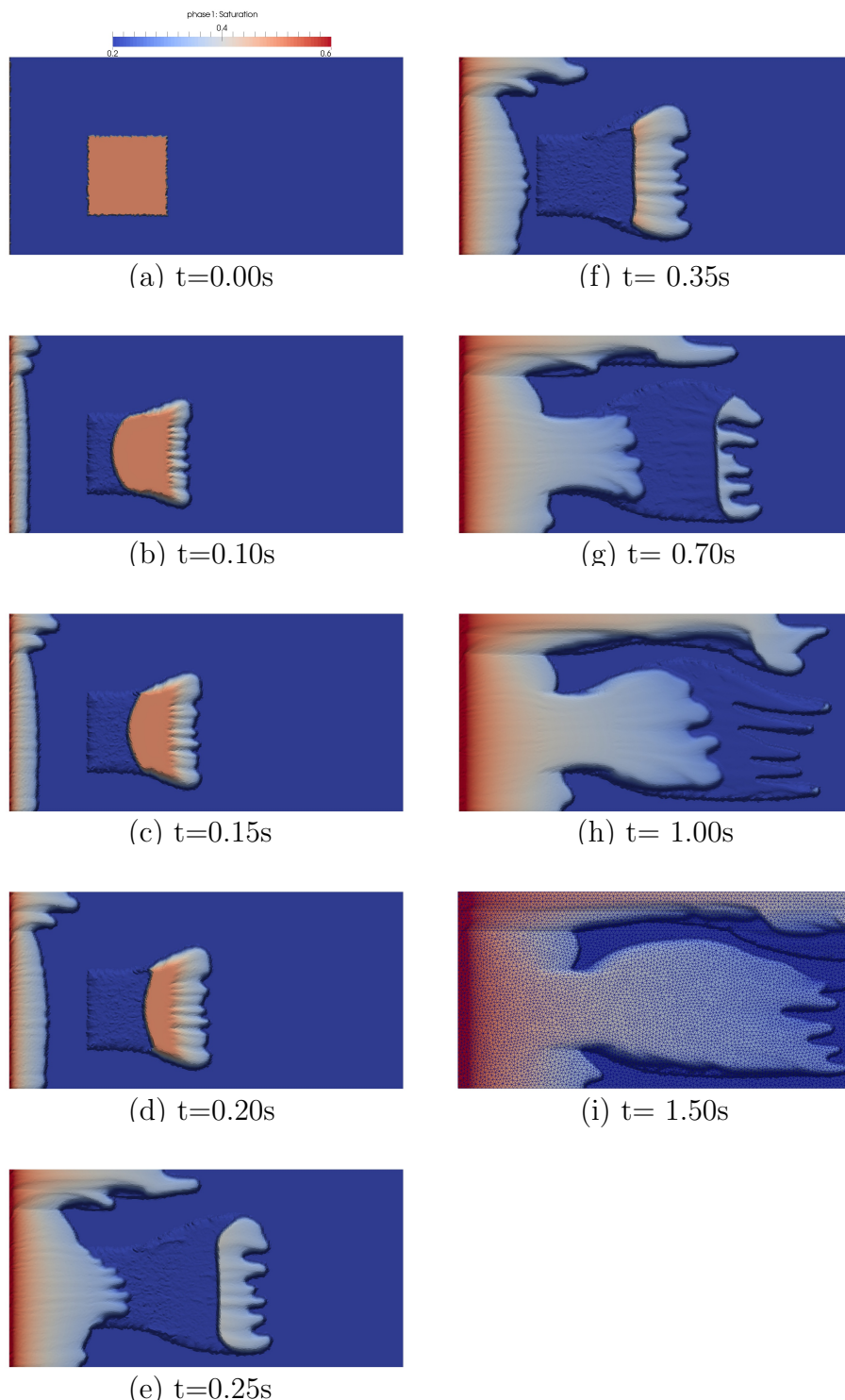


Figure 13: Impact of mesh resolution on capturing flow instabilities: snapshots of saturation field through 1.50 seconds of numerical simulation performed with fixed mesh (of 13068 elements) and  $VR=10$ .

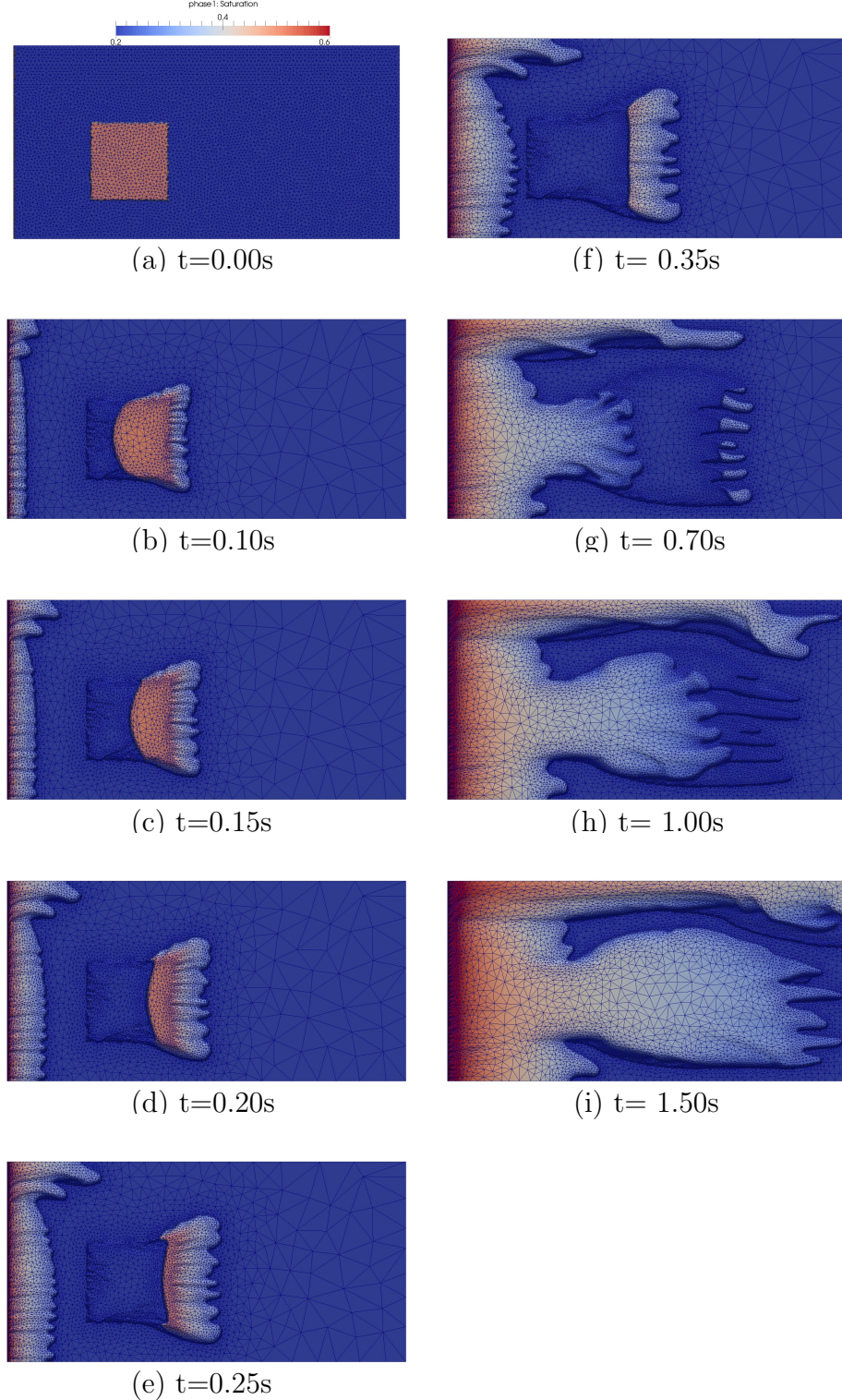


Figure 14: Impact of mesh resolution on capturing flow instabilities: snapshots of saturation field through 1.50 seconds of numerical simulation performed with adaptive mesh and  $VR=10$ .

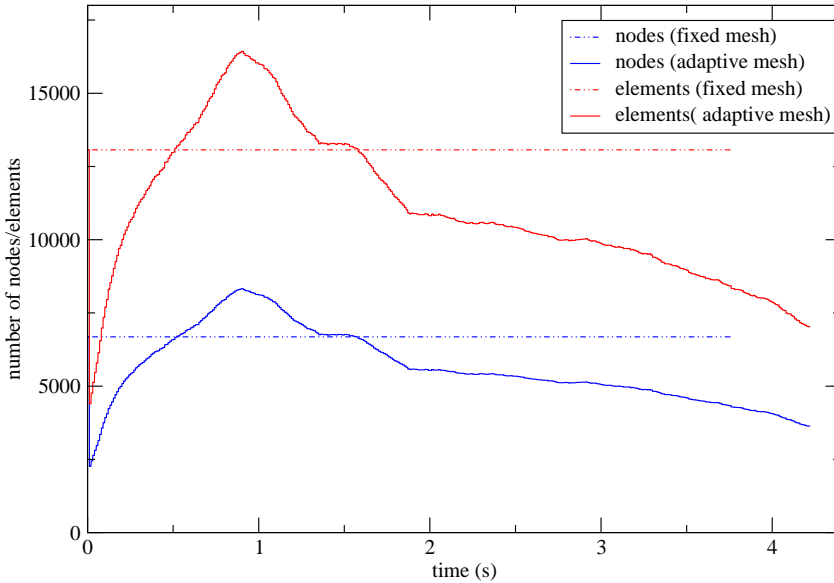
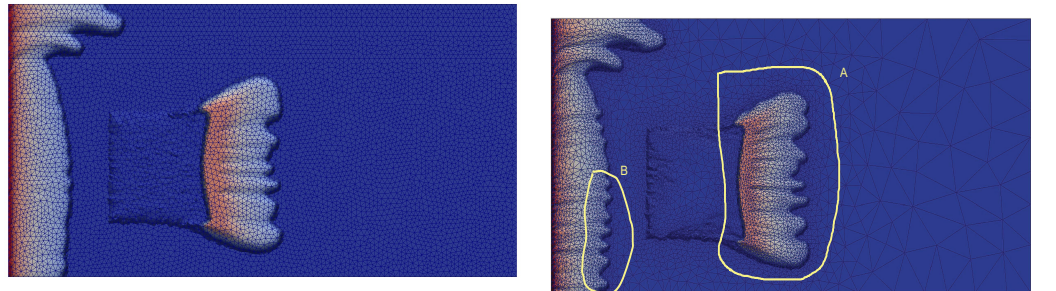
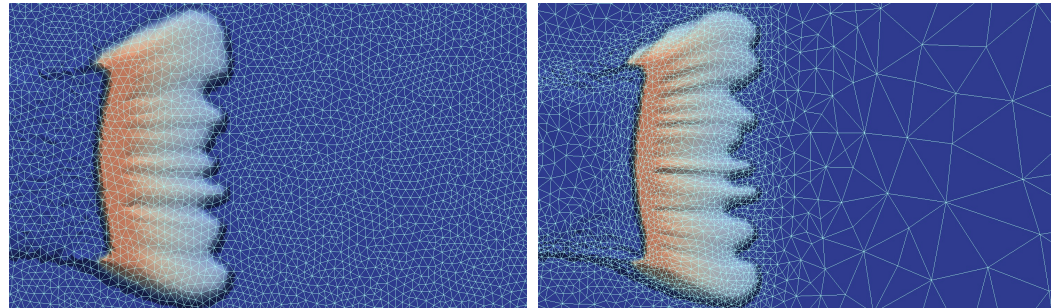


Figure 15: Impact of mesh resolution on capturing flow instabilities: total number of elements and nodes for simulations performed with fixed and adaptive mesh.



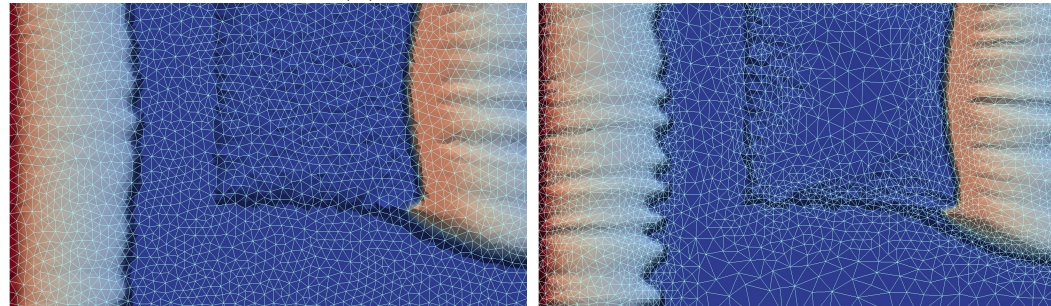
2531  
2532  
2533  
2534  
2535  
2536  
2537  
2538  
2539  
2540  
2541  
2542  
2543  
2544  
2545  
2546  
2547  
2548  
2549  
2550  
2551  
2552  
2553  
2554  
2555  
2556  
2557  
2558  
2559  
2560  
2561  
2562  
2563  
2564  
2565  
2566  
2567  
2568  
2569  
2570  
2571  
2572  
2573  
2574  
2575  
2576

(a) fixed and adaptive mesh



2541  
2542  
2543  
2544  
2545  
2546  
2547  
2548  
2549  
2550  
2551  
2552  
2553  
2554  
2555  
2556  
2557  
2558  
2559  
2560  
2561  
2562  
2563  
2564  
2565  
2566  
2567  
2568  
2569  
2570  
2571  
2572  
2573  
2574  
2575  
2576

(b) Zoom on region *A*



2551  
2552  
2553  
2554  
2555  
2556  
2557  
2558  
2559  
2560  
2561  
2562  
2563  
2564  
2565  
2566  
2567  
2568  
2569  
2570  
2571  
2572  
2573  
2574  
2575  
2576

(c) Zoom on region *B*

2563  
2564  
2565  
2566  
2567  
2568  
2569  
2570  
2571  
2572  
2573  
2574  
2575  
2576

Figure 16: Impact of mesh resolution on flow instabilities: capturing formation and growth of flow instabilities at fluid interfaces ( $t = 0.20$  s) in two regions of the computational domain, *A* and *B*. Simulations were conducted with fixed (left-hand side) and adaptive meshes.

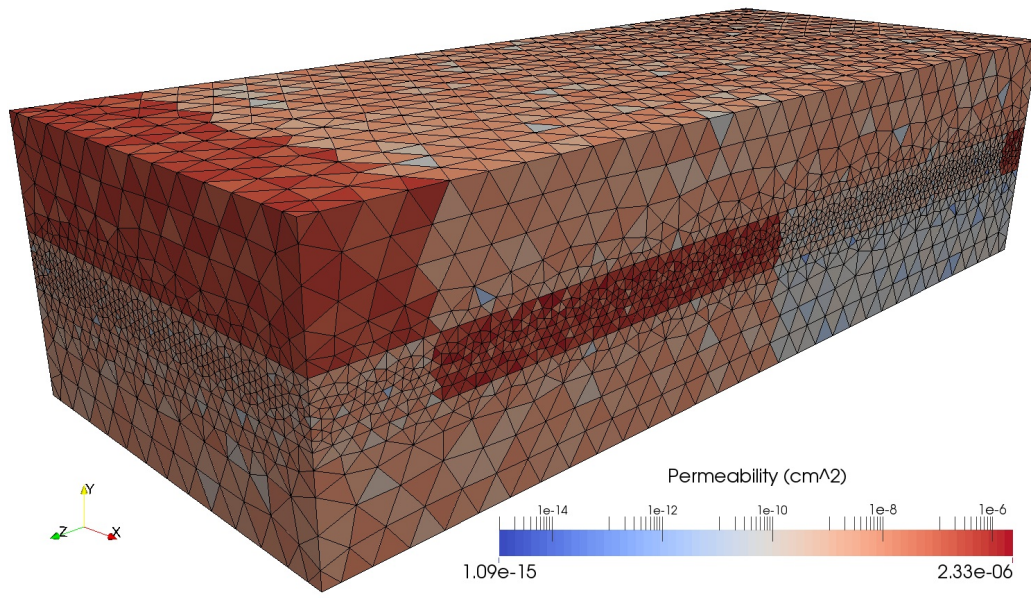
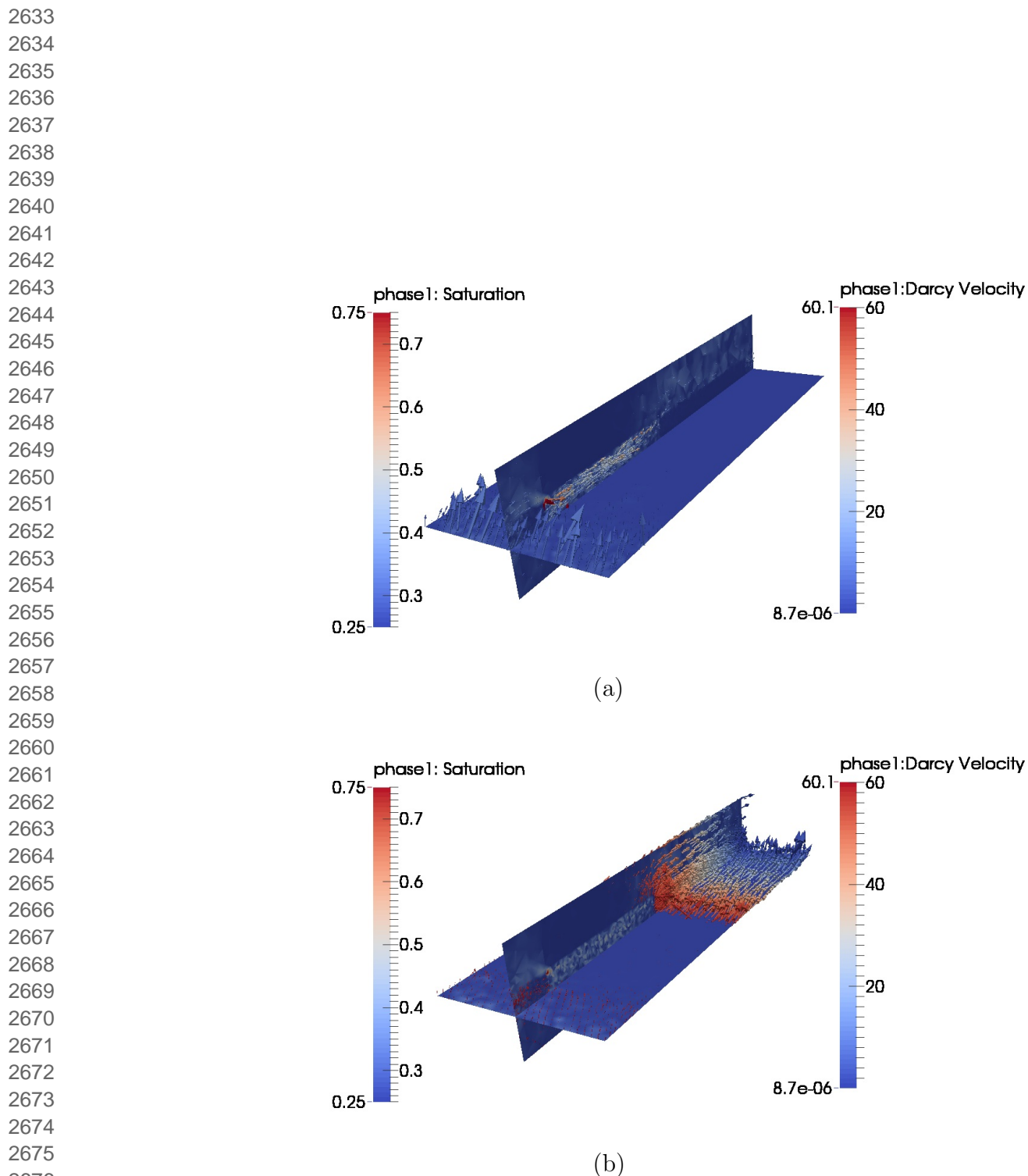
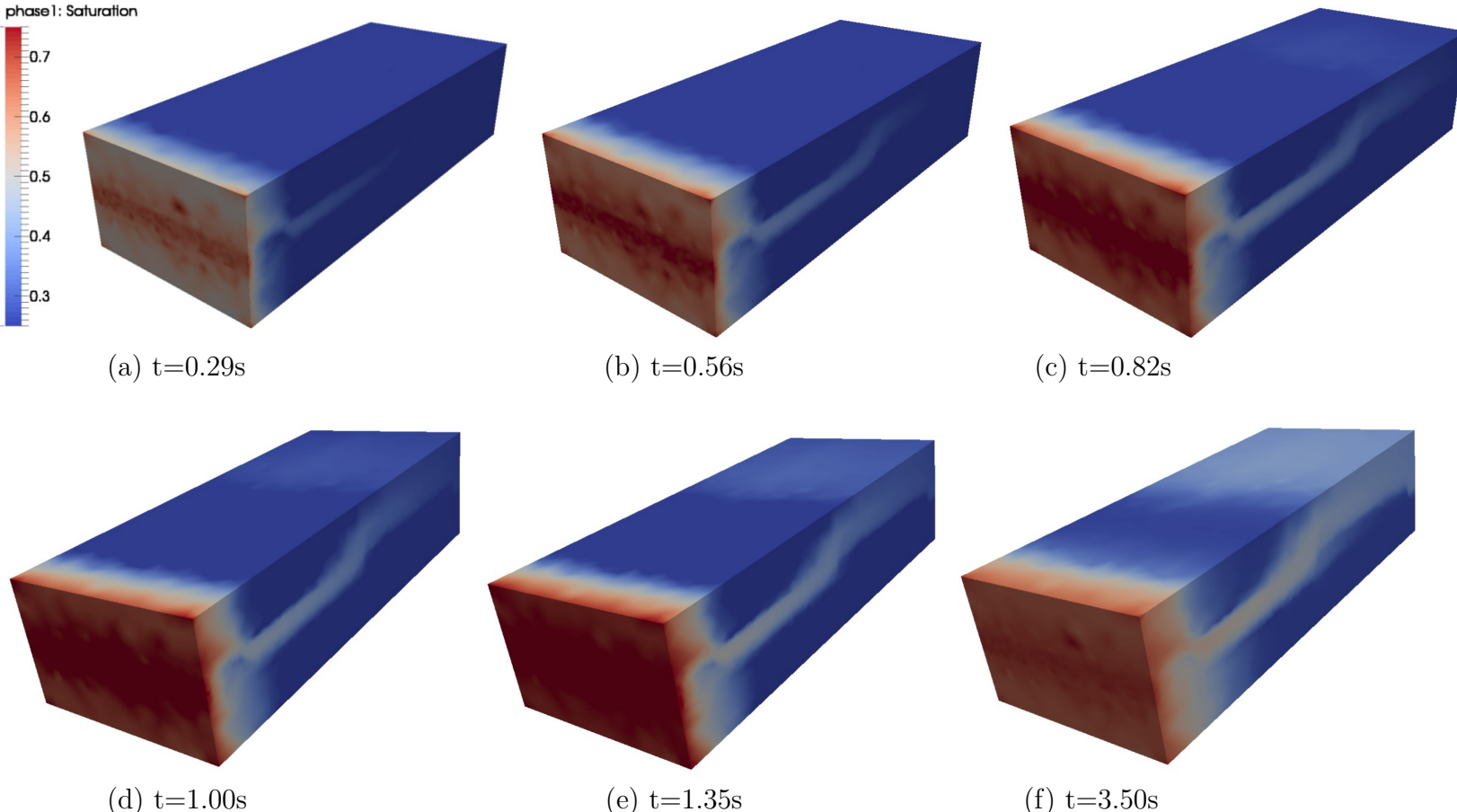


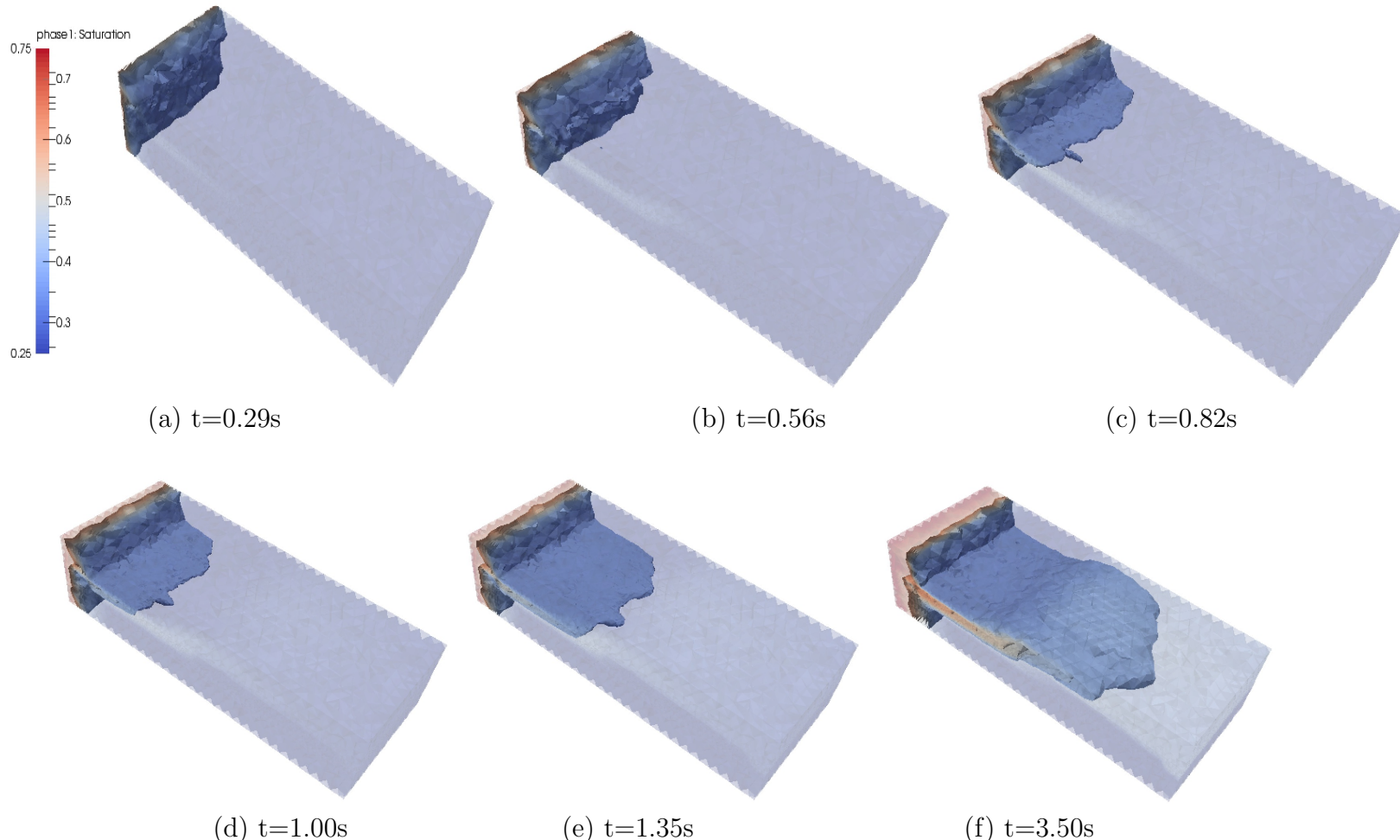
Figure 17: 3D channel flow (fixed mesh): permeability distribution. The domain contains 243056 P<sub>1</sub>DG-P<sub>1</sub> element-pairs.



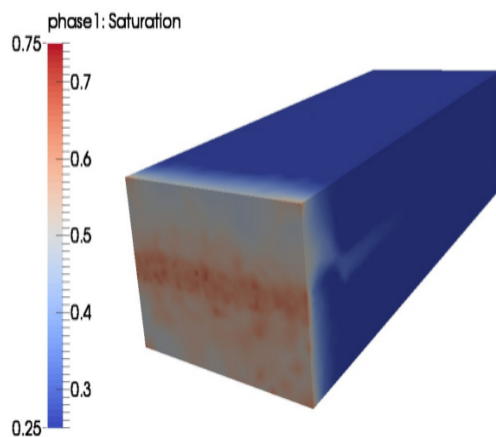
2677 Figure 18: 3D channel flow (fixed mesh): XY and YZ planes showing wetting fluid  
 2678 phase Darcy velocity vectors overlapped with wetting fluid saturation at (a) t=0.29s and  
 2679 (b)t=4.3s.  
 2680  
 2681  
 2682  
 2683  
 2684  
 2685  
 2686  
 2687  
 2688

2689  
2690  
2691  
2692  
2693  
2694 phase1: Saturation  
2695 0.75  
2696 0.7  
2697 0.6  
2698 0.5  
2699 0.4  
2700 0.3  
2701 0.25  
2702  
2703  
2704  
2705 (a) t=0.29s  
2706 (b) t=0.56s  
2707 (c) t=0.82s  
2708  
2709  
2710  
2711  
2712  
2713  
2714  
2715  
2716  
2717  
2718  
2719 Figure 19: 3D channel flow (fixed mesh): saturation front evolving in time and space with preferential flow pathways through  
2720 3.50 seconds of numerical simulations. Preferential flow pathway can be readily noticed in these frames, mirroring permeability  
2721 distribution. The domain contains 368513 P<sub>1</sub>DG-P<sub>1</sub> elements.  
2722  
2723  
2724  
2725  
2726  
2727  
2728  
2729  
2730

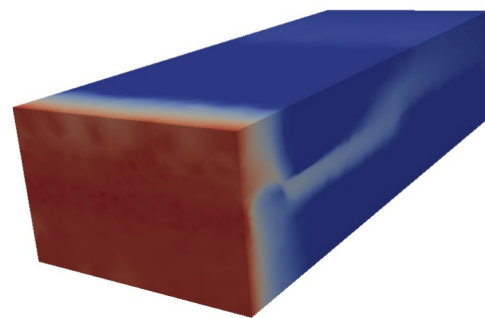




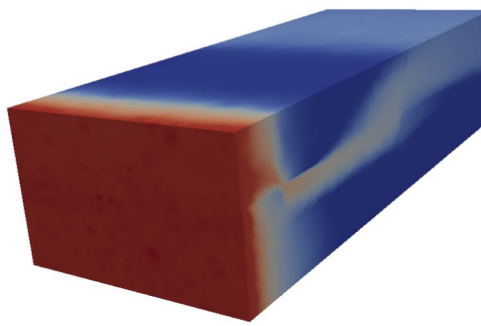
2765 Figure 20: 3D channel flow (fixed mesh): Isosurfaces for wetted phase saturation ranging from 0.45 and 0.60 at the same  
2766 instants of time of Fig. 19. Preferential flow pathway can be readily noticed in (b) and (f). Fingers' formation and growth can  
2767 be clearly noticed in (b)-(e). The domain contains 368513 P<sub>1</sub>DG-P<sub>1</sub> elements.



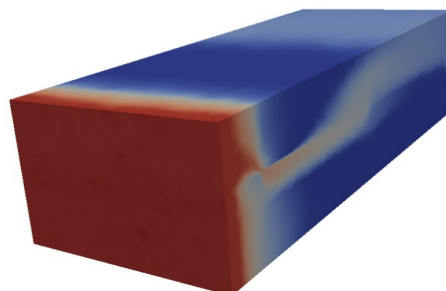
(a)  $t=0.29\text{s}$



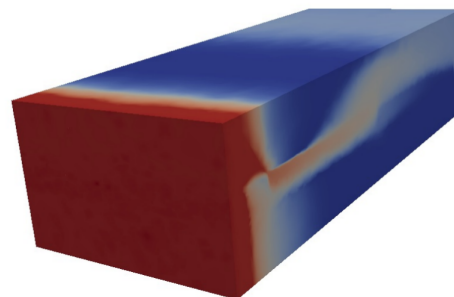
(b)  $t=0.56\text{s}$



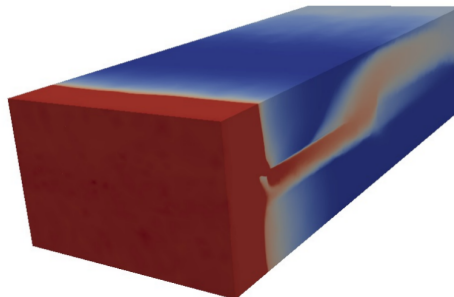
(c)  $t=0.82\text{s}$



(d)  $t=1.00\text{s}$



(e)  $t=1.35\text{s}$



(f)  $t=3.50\text{s}$

Figure 21: 3D channel flow (adaptive mesh): numerical simulation was performed with the smae boundary and initial conditions as in Figs. 17-20 with an adaptive mesh. Flow pathway is very similar to the one shown in Fig. 19.

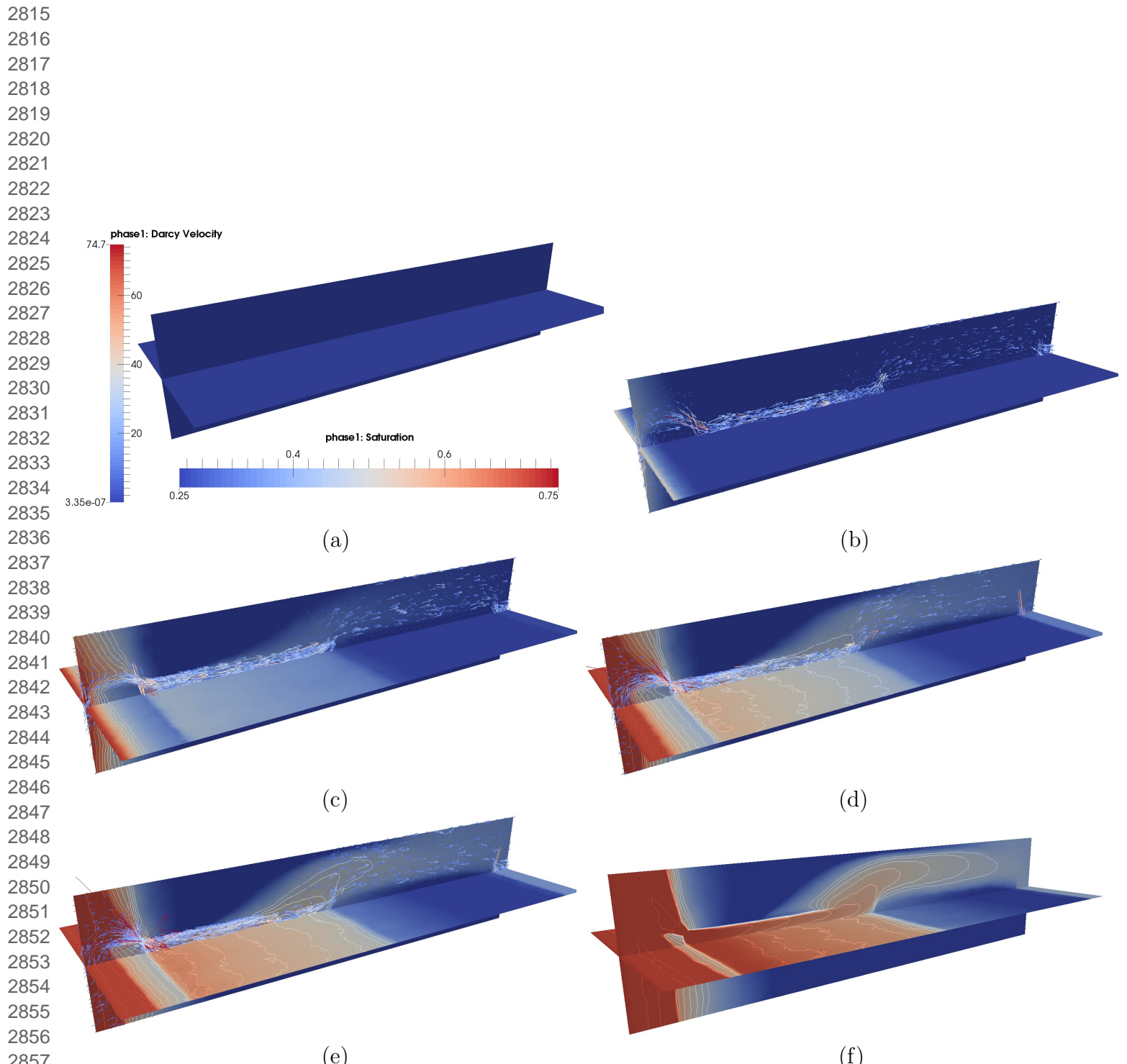


Figure 22: 3D Channel (adaptive mesh): XY and YZ planes showing wetting fluid saturation overlapped with Darcy velocity vectors at (a) 0.00, (b) 0.09, (c) 0.71, (d) 1.75, (e) 2.47 and (f) 3.78s. Colour scheme for saturation profile is the same as used in Fig. 21.

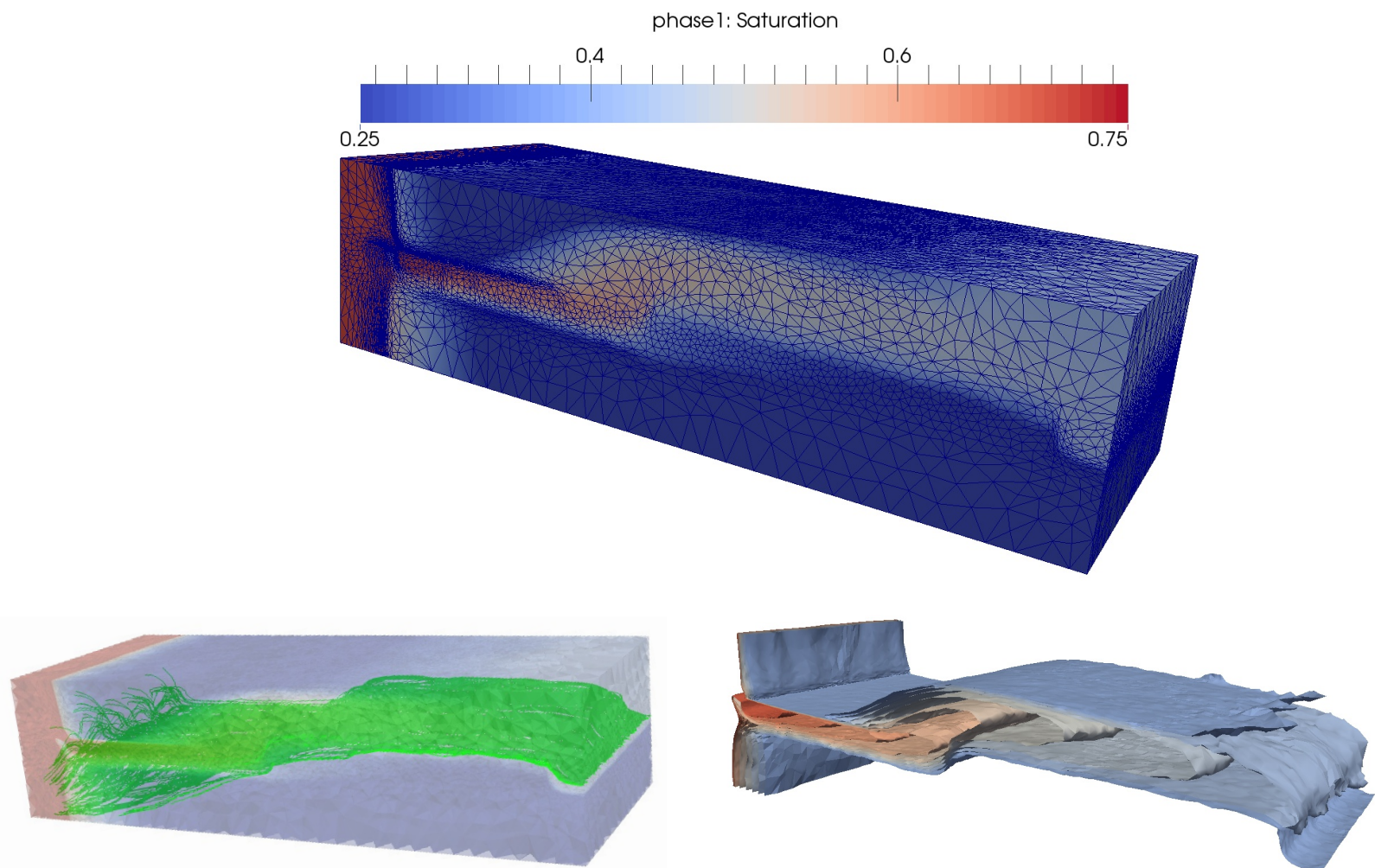


Figure 23: 3D Channel: Text to come